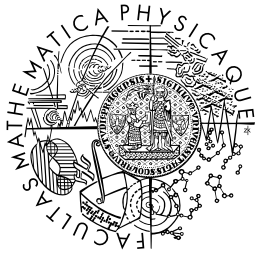

FACULTY
OF MATHEMATICS
AND PHYSICS
Charles University

BACHELOR THESIS

Radek Jirásek

Electroweak bosons as probes of quark-gluon plasma

Institute of Particle and Nuclear Physics

Supervisor of the bachelor thesis: Mgr. Martin Rybář, Ph.D

Study programme: Physics

Study branch: Physics

Prague 2023

I declare that I carried out this bachelor thesis independently, and only with the cited sources, literature and other professional sources. It has not been used to obtain another or the same degree.

I understand that my work relates to the rights and obligations under the Act No. 121/2000 Sb., the Copyright Act, as amended, in particular the fact that the Charles University has the right to conclude a license agreement on the use of this work as a school work pursuant to Section 60 subsection 1 of the Copyright Act.

In ..... date ....

Author's signature

I want to thank my supervisor, Martin Rybář, for his excellent advice and patience. I feel genuine gratitude to him for introducing me to this branch of particle physics in which I wrote this thesis. I would also like to thank my family and girlfriend Eva for their support.

Title: Electroweak bosons as probes of quark-gluon plasma

Author: Radek Jirásek

Department: Institute of Particle and Nuclear Physics

Supervisor: Mgr. Martin Rybář, Ph.D, Institute of Particle and Nuclear Physics

Abstract: This thesis is focused on heavy-ion physics which aims to improve our understanding of the strong interaction as well as of the quark-gluon plasma. Such an exotic state of matter exists only in the extreme conditions which could be achieved in the lead-lead collisions in the LHC at CERN. Hence we will discuss the physics of accelerators and detectors. We will outline the structure and properties of the ATLAS experiment, one of the detectors on the LHC. Later, we aimed at the physics behind the heavy-ion collisions. We describe what the quark-gluon plasma is and how we can use electroweak bosons to probe it. Basic of our analysis procedures will be introduced, as well as the principles of simulation of data with the Pythia8 model. The main goal of this work is to study the re-clustering of the jets and how that changes their properties. Then we focused on the properties of the electroweak bosons and how they could help us with the study of the quark-gluon plasma. In the end, we estimate the number of events that could be expected to observe in future measurements on ATLAS in heavy-ion collisions.

Keywords: ATLAS, quark-qluon plasma, electroweak bosons, jet, jet quenching

Název práce: Elektroslabé bosony jako nástroj pro studium kvark-gluonového plazmatu

Autor: Radek Jirásek

Katedra: Ústav částicové a jaderné fyziky

Vedoucí bakalářské práce: Mgr. Martin Rybář, Ph.D, Ústav částicové a jaderné fyziky

Abstrakt: Fyzika srážek těžkých iontů se zabývá otázkami silné interakce a studiem kvark-gluonového plazmatu. Extrémních podmínek potřebných pro vznik tohoto exotického skupenství látky se dá dosáhnout například ve stážkách jader olova na urychlovači LHC v CERNu. Proto v první kapitole budeme diskutovat právě urychlovače a detektory, jak fungují a jaké se především používají v experimentu ATLAS, který je jedním z detektoru na LHC. Dále se zaměříme na fyziku v pozadí těžko-iontových srážek, co to kvark-gluonová plazma je a jak ji lze zkoumat pomocí elektroslabých bosonů. Představíme také základní nástroje analýzy, které v práci používáme a postup simulace dat pomocí Pythia8 softwaru. Dále se zabýváme znovu-klastrováním jetů a jak tato procedura ovlivní vlastnosti jetů. Poté diskutujeme vlastnosti elektroslabých bosonů a jak je lze využít ke studiu kvark-gluonového plazmatu. Na závěr jsme pomocí simulací odhadli, jaké počty jetových událostí o určitých hybnostech lze očekávat v následujících měřeních na ATLAS detektoru pro těžko-iontové srážky očekávat.

Klíčová slova: ATLAS, kvark-gluonová plazma, elektroslabé bosony, jet, potlačení jetů

Contents

Introduction

The Large Hadron Collider, situated at CERN, is probably one the most prominent scientific projects of mankind. With the usage of detectors, scientists research the most elementary aspects of our reality, the building blocks of matter, and the interactions between them. The exotic state of matter is created when heavy nuclei of atoms are smashed together with enough energy, which is being studied on detectors at the Large Hadron Collider as well. This phase of matter, predicted by Quantum Chromodynamics, is called the Quark-gluon plasma and was probably present in the earliest Universe short after the Big Bang.

The suppression of the production of some particles is observed in the quark-gluon plasma. That processes indicate the behavior of the medium as well as the properties of strong interaction itself. One of the manifestations of the medium is jet quenching, a suppression of collimated sprays of particles originating from the fragmentation of fast partons. We will focus on the hadron decay channel of electroweak bosons because these create jets that subsequently interact with the quark-gluon plasma. For the reason of the presence of large background in such measurement, electroweak bosons have not been well studied in that channel. With the usage of simulation, we will analyze the behavior of the Z and W bosons and the options for re-clustering jets to improve our detection. With the simulation, we can predict the number of processes we will see in the future measured data with higher energy in head-on-collision. That could be useful, considering the increase of beam energy in heavy-ion run on LHC this year.

First, we will get to know the basic properties of the detection setup used in the LHC, particularly at the detector ATLAS. Providing elemental information about the process of how the particles are detected. Later in the thesis, we focus on the physics background and, more significantly, on the quark-gluon plasma, what it is, and how it behaves, as well as the properties of the jets and interaction with that plasma.

1. Experimental setup

1.1 Physical quantities

Among quantities describing experimental setup in particle physics belong luminosity. The instantaneous luminosity $\mathcal{L}$ describes the rate how many events a collider generates per second, and the formula for it could be denoted as:

$$\mathcal{L} = \frac{1}{\sigma}\frac{dN}{dt}\,, \tag{1.1}$$

where N is number of observed events with at given cross-section σ of that process. The performance of the accelerator is usually characterized by instantaneous luminosity for all inelastic interactions. The σ is then the total inelastic cross-section. Integrated luminosity L is instantaneous luminosity integrated over a defined period of time:

$$L_t = \int_0^t \mathcal{L} d\tau\,. \tag{1.2}$$

From (1.1) we can derive formula for number of events N_p of given process 'P' with same cross-section σ_p over time t as:

$$N_p = L_t \sigma_p\,. \tag{1.3}$$

Given by the Special theory of relativity (STR), the kinematic state of a particle is described by a four-vector of momentum P^μ. The scalar product $P^\mu P_\mu$ [1] is equal to the invariant:

$$m^2 = P^\mu P_\mu = E^2 - p^2 \tag{1.4}$$

where m is the invariant mass of the particle, E is the particle's energy, and p is the size of the momentum vector $\mathbf{p}$. Similarly, we can denote the center-of-mass energy as:

$$\sqrt{s} = \sqrt{P^\mu P_\mu} = \sqrt{(E_1 + E_2)^2 - (\vec{p_1} + \vec{p_2})^2}\,, \tag{1.5}$$

where indexes 1 and 2 denote corresponding quantities of particle number one and particle number two, respectively, and $\vec{p_i}$ is the three-vector of momentum of an i-th particle. The center-of-mass energy is frequently used to determine adequate energy in a particle collision.

1.2 Large Hadron Collider

The European Organisation for Nuclear Research, CERN, located at the border between Switzerland and France, is the world's largest and most respected center for research in nuclear and particle physics. The main aim of interest of

[1] The Minkowski metric tensor is used with notation (1,-1,-1,-1). We use notation where an upper index is used with vectors, and a lower index is used with covectors.

CERN is focused on elementary research. At CERN, there are currently many ongoing research projects using a variety of particle accelerators of different energies. The most famous is LHC, a large hadron collider with four multipurpose experiments: ATLAS, ALICE, CMS, and LHCb. Besides, there are experiments with a fixed target like COMPASS or CLOUD, anti-matter experiments like ALPHA or AEGIS, experimental facilities like ISOLDE, and non-accelerator experiments like AMS [1].

LHC is 27 km long and a circular-like a shape collider situated 100 m deep underground on average. Regarding the proton-proton collisions, two beams of up 2838 bunches of particles are accelerated in the LHC. Every bunch contains more than $1.2 \cdot 10^{11}$ protons [2]. Many smaller colliders have been used to accelerate particles up to energies that can be further increased in LHC. For example, before particles could be injected into LHC, they have been accelerated up to 450 GeV[2] in SPS (Super Proton Synchrotron). A diagram of the layout of the colliders can be seen in the picture in Figure 1.1:

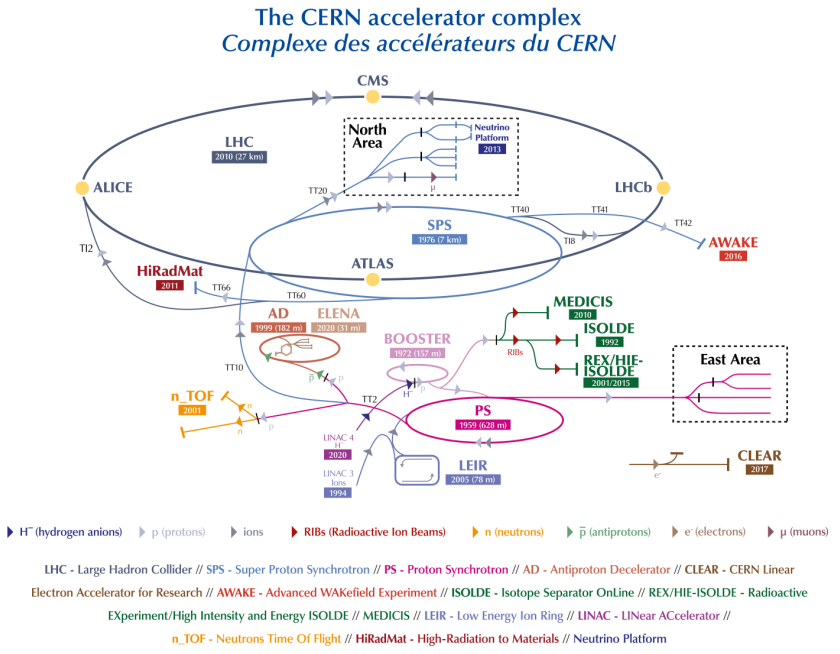

Figure 1.1: Diagram of the layout of the accelerators at CERN. [2]

There are mainly two types of accelerators. First, circular accelerators, the same type as LHC, have a significant advantage in an opportunity to accelerate identical particles many times. Therefore, the energy increase per circulation could be minimal, and we can achieve the highest energy of particles with this type of collider. The main disadvantage of the circular collider is the energy loss of particles due to the continual changing of their trajectories. Every charged particle subjected to changing direction emits energy via the electromagnetic field. This effect, called Synchrotron radiation, is highly dependent on particle

[2]We use standard units in particle physics, electron-volts. A particle with elementary charge e gains 1 eV of energy by accelerating in the potential of 1 V.

rest mass. We can denote energy loss via this process as [3]:

$$\frac{dE}{dt} = \frac{1}{6\pi\varepsilon_0}\frac{e^2 c}{r^2}\beta^4\gamma^4\,, \tag{1.6}$$

where c is the speed of light, e is the elementary charge, r is the radius of the accelerator (assuming circular shape), and β=v/c, $\gamma = (1 + E/m)$ are classic STR quantities. The heavier the particle, the less energy loss via this effect. Therefore, protons or heavy ions are mainly used in circular accelerators. The second disadvantage is that a strong magnetic field has to be used to keep high energy particles on circular trajectories. This is currently the main limiting factor. A second type, a linear accelerator, is built in a straight line. Particles in this type of accelerator have collided with the target or another bunch of particles without any option to repeat acceleration. The main advantage of this type of accelerator is the absence of energy losses due to synchrotron radiation. Therefore, linear accelerators could accelerate particles as electrons. Since electrons are elementary particles without structure, meaning we can specify the energy of products before and after the collision in all three spatial dimensions, apart from an example with protons where the parton distribution function (PDF) played a significant role in this problem. We will discuss Parton distribution functions more in the next chapter 2.1. Having two bunches of particles accelerated in opposite directions is highly convenient for energy in their collision. We can see from equation (1.5) that the center-of-mass energy is maximum in that case. The center-of-mass energy was $\sqrt{s} = 13\,\text{TeV}$ in LHC during run 2 in the proton-proton collisions[2]. In the lead-lead collisions, the center-of-mass energy was $\sqrt{s_{NN}} = 5.02\,\text{TeV}$ in LHC during run 2 [2]. This year, during run 3, $PbPb$[3] nuclei will be collided together with the center-of-mass energy $\sqrt{s_{NN}} = 5.36\,\text{TeV}$.

1.3 Detectors at LHC

Large detectors in particle physics are made of several sub-detectors and sub-systems. Each sub-system has specific properties to detect different types of particles. Typically, the closest layers to the collision center detect the trajectories of charged particles. This section of the detector is essential for measuring the momentum of charged particles. The subsequent layers detect the position and energy of particles in destructive ways. Therefore, the detector must consist of such layers to ensure particles with a short life or substantial energy loss will be safely detected. Outer layers should be focused on detecting particles that barely interact with the detector. The interaction of particles with an individual layer of a detector can be seen in the figure 1.2.

[3]This year will also be used nuclei of oxygen to study properties of collisions with a smaller number of nucleons.

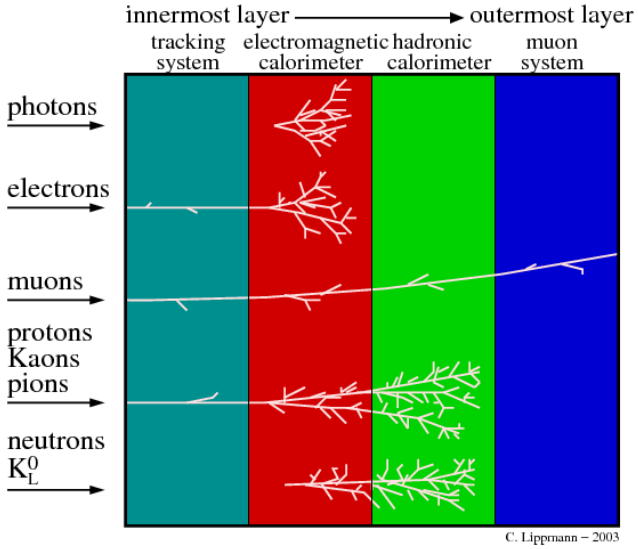

Figure 1.2: Schematic representation of particle interaction in each detector layer. [4]

There are four main detectors on LHC, ALICE, ATLAS, CMS, and LHCb. ALICE (A Large Ion Collider Experiment) is specialized in heavy ion collisions and studies of quark-gluon plasma. Detector LHCb is specialized in b physics, which means physics focused on the bottom quark and with that connected CP violation. More about particles will be discussed in chapter 2.1. Detectors CMS (Compact Muon Solenoid) and ATLAS (A Toroidal LHC ApparatuS) are general-purpose experiments.

1.4 ATLAS detector

The highest instantaneous luminosity of run 2 in ATLAS was achieved in late 2018 in the proton-proton collisions $\mathcal{L}_{2018-pp} = 21 \cdot 10^{33}\,\mathrm{cm}^{-2}\mathrm{s}^{-1}$ [5] with $\sqrt{s} = 13\,\mathrm{TeV}$. In the same year, the highest instantaneous luminosity in the lead-lead collisions was $\mathcal{L}_{2018-PbPb} = 6.2 \cdot 10^{27}\,\mathrm{cm}^{-2}\mathrm{s}^{-1}$ with $\sqrt{s_{NN}} = 5.02\,\mathrm{TeV}$ [5]. During run 2 (only $\sqrt{s} = 13\,\mathrm{TeV}$, proton-proton collisions), ATLAS recorded the total integrated luminosity $L_{run2} = 147\,\mathrm{fb}^{-1}$[5]. At the end of the year 2022, $\mathcal{L}_{2022-pp} = 23.9 \cdot 10^{33}\,\mathrm{cm}^{-2}\mathrm{s}^{-1}$ with $\sqrt{s} = 13.6\,\mathrm{TeV}$ [6] has been achieved.
The ATLAS detector can be divided into four main subcategories or layers. Each layer is denoted by some color in the figure 1.3. The whole detector is symmetric with respect to the plane perpendicular to the beamline and passing through the collision point.

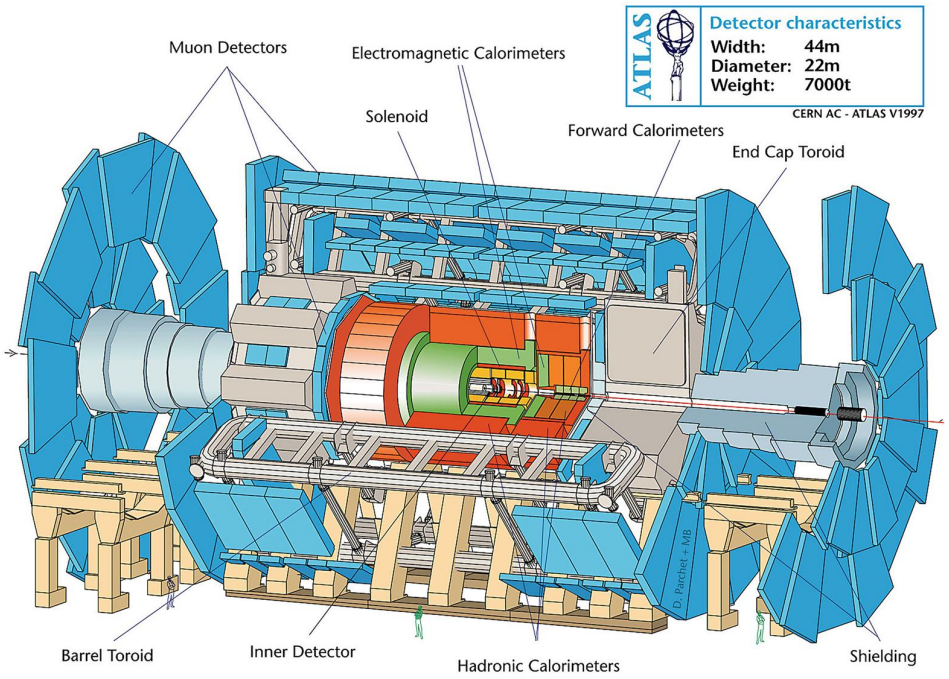

Figure 1.3: Diagram of the ATLAS detector. [7]

1.4.1 ATLAS coordinate system

The coordinate system of the ATLAS detector is a right-handed coordinate system with the z-axis pointing along the tunnel and the x-axis pointing toward the center of the LHC. The coordinate system can be seen in the diagram Fig. 1.4.

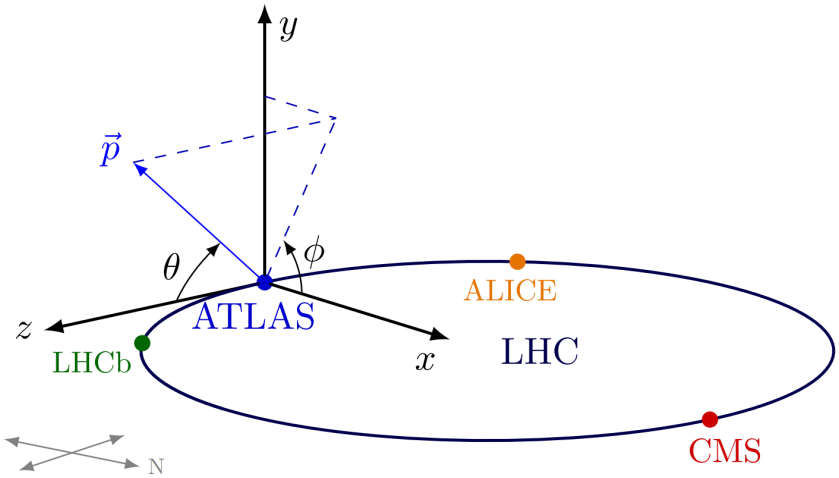

Figure 1.4: Diagram of ATLAS coordinate system. [8]

We will now define several kinematic variables that are commonly used in particle physics and also in this work. Let us define transverse components of kinematics quantities by simple trigonometric functions as like as

$$\begin{aligned} p_{\mathrm{T}} &= p\sin(\theta) \\ E_{\mathrm{T}} &= E\sin(\theta)\,. \end{aligned} \tag{1.7}$$

A beneficial quantity in relativistic physics is rapidity y. Rapidity can be defined as [9]:

$$y = \frac{1}{2} \ln \left(\frac{E + p_z}{E - p_z} \right) . \tag{1.8}$$

The most significant advantage of using rapidity in relativistic physics is that rapidity is additive, unlike velocity. In particle physics, we define so-called pseudorapidity for avoiding problems with complicated measurements of large z-component of the momentum. If we assume limit $E \approx p$ than we can write equation (1.8) as:

$$y \approx \frac{1}{2} \ln \left(\frac{p + p_z}{p - p_z} \right) = \frac{1}{2} \ln \left(\frac{1 + \cos(\theta)}{1 + \cos(\theta)} \right) . \tag{1.9}$$

Then if we use the trigonometric formula for halve argument, we get pseudorapidity η:

$$\eta = -\ln \left(\tan \frac{\theta}{2} \right) \tag{1.10}$$

The next useful quantity in particle physics is ΔR,

$$\Delta R = \sqrt{(\Delta\eta)^2 + (\Delta\phi)^2}. \tag{1.11}$$

ΔR is the distance of some objects in the space of η and ϕ and is used for analysis and calibrations or tagging of jets, for example.

1.4.2 The inner tracker

The innermost part of the layout is the inner tracker. This subdetector measures the trajectories of charged particles via several methods.

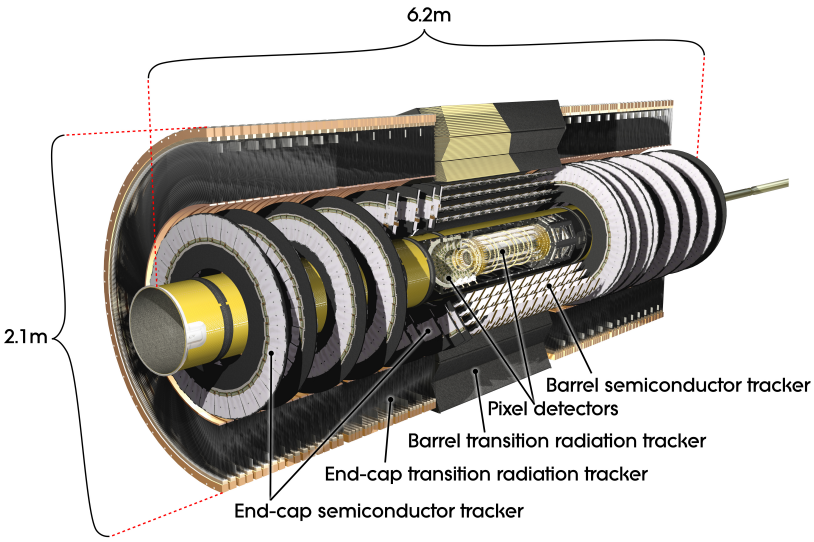

Figure 1.5: Diagram of the inner tracker of ATLAS detector. [10]

The inner tracker has three parts [11]. These parts can be seen in figure 1.4. The first sub-system uses semiconductor pixel sensors to detect the point where charged particles go through the detector. The point where the particle hits the sensor is measured with a precision of almost 10 μm. There are more than 92 million pixels in two segments—the first, four barrel-like layers around the beam line of LHC. The closest one is only 3.3 cm from the beam line. The second segment has three disks in each end-cap part of the detector. Dimensional proportions and pseudorapidity coverage of each part of the inner tracker can be seen in the figure 1.5. The second part of the inner tracker is Semiconductor

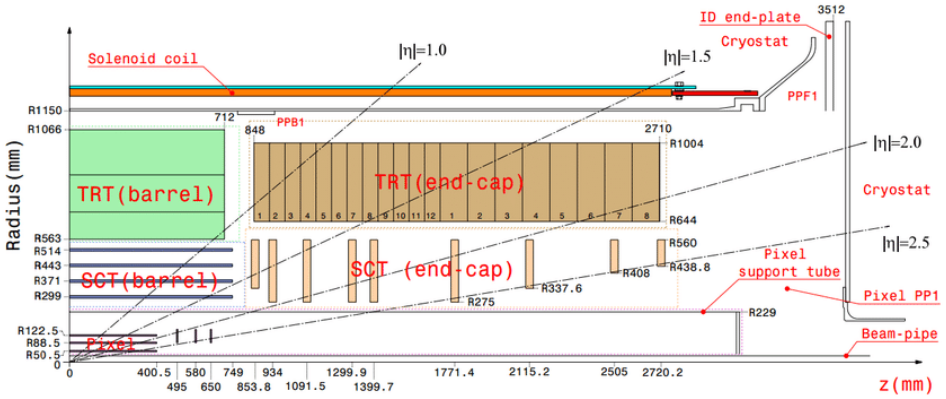

Figure 1.6: The schematic picture of inner detector of the ATLAS, viewed in the r-z plane, where r is the radial distance from the z-axis. [12]

Tracker (SCT) consists of over 4000 modules made up of 6 million strips in total. The sensor is made up of an extremely pure silicon monocrystal doped on each side with specific elements to create a diode. The sensor as a diode is connected to high voltage in a closed direction. Hence almost no electrical current flows. In the case that an electrically charged particle flies through the sensor, silicon is ionized, and the newly created charge in the depletion region starts moving in the direction corresponding to electric potential. Therefore each sensor has many aluminum strips on the surface used for the discharge doped silicon part. Diagram of proportion of the sensor can be seen figure 1.6

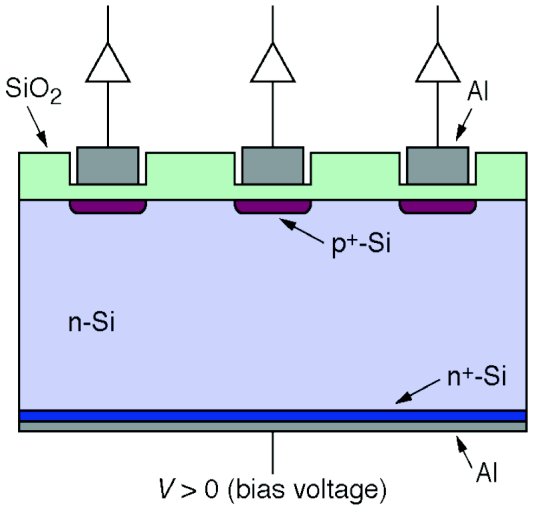

Figure 1.7: Schematic view of semiconductor silicon strip sensor. [13]

The third part of the inner detector is Transition Radiation Tracker (TRT). This sub-system comprises 300 000 thin-walled drift tubes. Tubes are filled with a gas mixture and have gold-plated tungsten wire in the center. A charged particle crossing the tube ionizes the gas, creating a detectable electric signal. Besides that, particles emit so-called transition radiation between the tubes. This radiation provides rough information about the particle's mass, which is especially important for recognizing electrons.

Computing algorithms merge this information in each layer and create one trajectory for every individual particle.

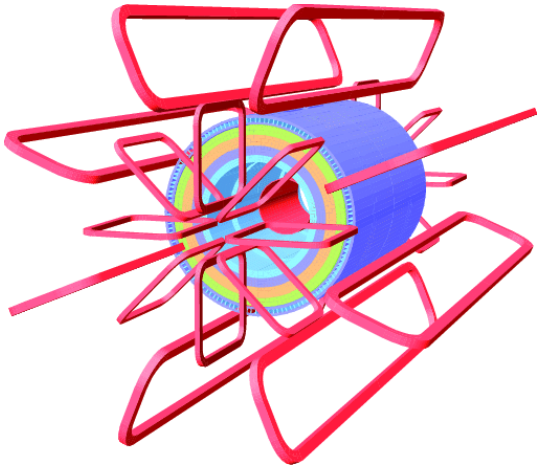

Figure 1.8: Schematic representation of the ATLAS magnetic system. Ping color denotes the magnet system itself, and other colors denote components of the calorimeter perturbating the magnetic field.[14]

1.4.3 Magnetic field

A magnet system generates a strong magnetic field in the detector, which bends the trajectories of the particles. Thanks to that, data from the Inner tracker can provide information about the particle's momentum going through the detector. Let us assume an equation of a stationary magnetic field oriented perpendicular to the particle's movement with electric charge q. Solving it for the momentum of the particle yields

$$F_m = qvB = \frac{mv^2}{r} = F_c \implies p = rqB\,, \tag{1.12}$$

where r is the measured radius of curvature, and B is the known magnetic induction of the magnetic field. This calculation simplifies the process, insomuch as the magnetic field is not homogeneous. We must know the magnetic field in every part of the detector for precise measurement. The total magnetic field in the detector cavity is computed as the superposition of the Biot-Savart contributions of all magnet windings [15]. Incredibly challenging is a simulation of perturbations of the magnetic field due to other ferromagnetic segments of detector layers, like the iron structure in the Tile calorimeter. In the ATLAS detector, two magnet systems are involved. First, Central Solenoid Magnet surrounds the inner tracker. It is 5.6 m long solenoid with diameter

2.56 m providing the magnetic field with magnetic induction 2 T in just 4.5 cm thickness. Second, the Toroid Magnet comprises three parts; two end-cap toroids with size 10.7 m in diameter, and a large barrel toroid with size20.1 m in diameter containing eight separate coils. The Toroid magnet provides a magnetic field with magnetic induction up to 3.5 T [16]. A schematic view of the ATLAS magnet system can be seen in the picture in Fig. 1.8.

1.4.4 Calorimeters

Calorimeters measure the energy of particles in destructive ways. They are designed to absorb most of the particles except muons and neutrinos. Calorimeters are made up of alternating layers of absorbing material stopping the particle and layers of "active" medium measuring the energy of the particle. A typical way of particle interactions with the absorbing layer is evolving into a particle shower, generating lots of particles. A schematic view of the ATLAS calorimeter system can be seen in Fig. 1.9 There are four main types of calorimeters. First, the Liquid Argon Colorimeter (LAr) surrounds the ATLAS Inner Detector and uses liquid argon as the active medium. LAr calorimeter is used both for electromagnetic and hadronic calorimeters and in central and more forward regions. An electromagnetic LAr calorimeter measures the energy of particles interacting via electromagnetic interaction, and this part of LAr is the closest to the center of detectors of all calorimeters.

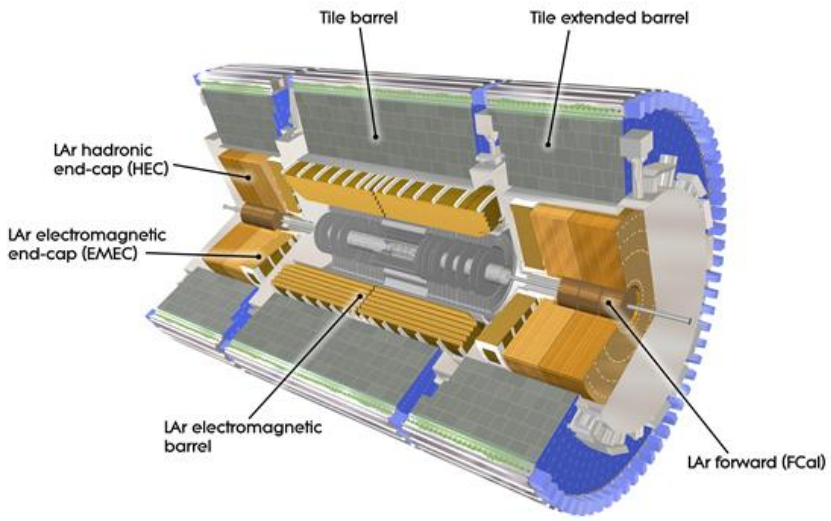

Figure 1.9: Schematic view of ATLAS calorimeter with notes of different parts.[17]

Different granularity is used through the volume to ensure the best distinguishing performance between particles. Electrons and photons generate an electromagnetic shower in the steel (absorbing layer of LAr calorimeter). Newly created particles ionize liquid argon, and copper wires read out electric charges. A schematic view of the LAr design of the calorimeter is displayed in Figure 1.11. [15].

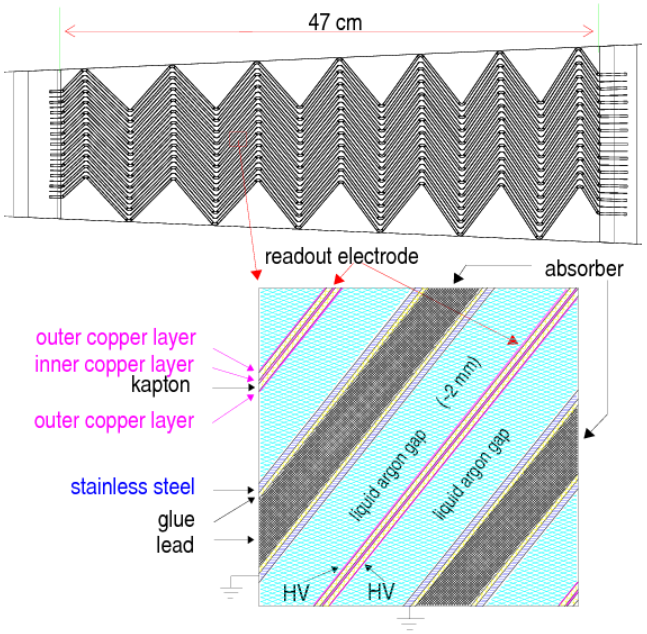

Figure 1.10: Diagram of ATLAS LAr calorimeter [18].

In the case of charged hadrons, they lose energy mainly by ionization in steel and thus create free electrons, which ionize liquid argon. Besides electromagnetic calorimeter, LAr technology is used in hadronic end-cap calorimeter (HEC) and forward calorimeter (FCal). The thickness of the detector in terms of interaction lengths depending on the pseudorapidity can be seen in the Fig. 1.10:

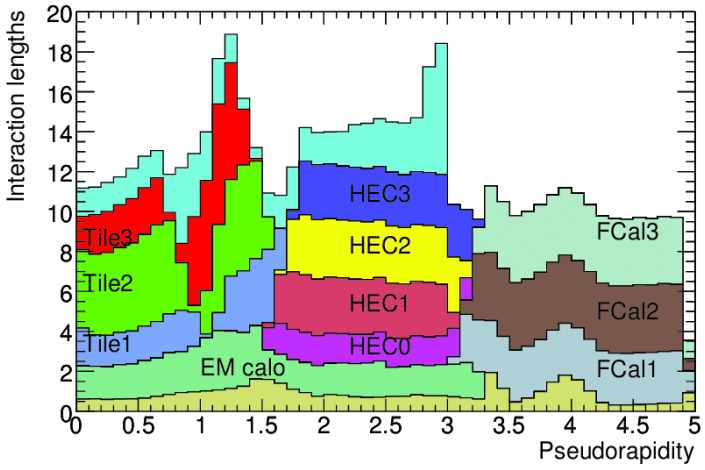

Figure 1.11: Graph of interaction lengths of detector layers depending on the pseudorapidity. [15].

The second type of technology is used in the hadronic Tile calorimeter. The tile calorimeter uses steel as the absorber and plastic scintillators as the active medium. Alternating layers are located in the region $|\eta| < 1.7$ normal to the beamline providing almost seamless azimuthal calorimeter coverage. Wave-length shifting fiber readout signal on the edge of the tile and grouping it together into the readout photomultiplier tubes. Fig 1.12 demonstrate the design and orientation of alternating absorber and active medium layers. 1.12:

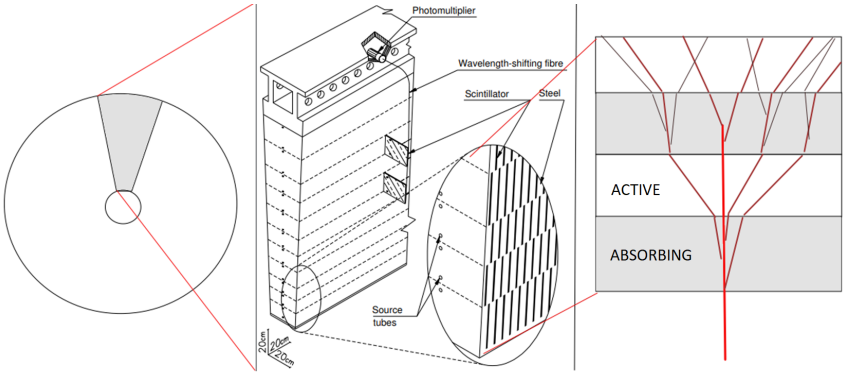

Figure 1.12: Diagram of ATLAS Tile calorimeter. From [19] (edited)

Another calorimeter used in ATLAS is ZDC (Zero Degree Calorimeter), providing coverage of region $|\eta| > 8.3$. It is located ± 140 m from the interaction point behind the separation of beams, where extreme radiation doses are present. The primary purpose of this calorimeter is to detect neutrons in a heavy-ion collision and determine the centrality of the collision.

Besides ZDC, there are more forward detectors. LUCID is a detector measuring relative luminosity in real time. It is located 17 m from the interaction point, which can be seen in Fig. 1.13. The third forward detector and most distant is ALFA. It is an absolute luminosity detector.

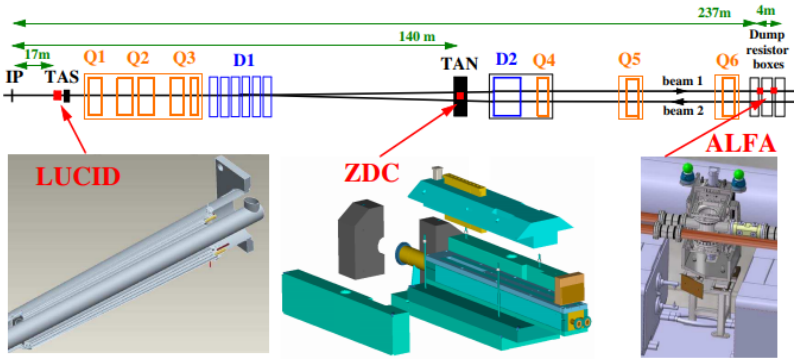

Figure 1.13: Schematic Figure of forward detectors and their locating in the beamline. [15]

In 2020, a new forward detector was been added to the ATLAS, the AFP (The Atlas Forward Proton detector). AFP aims to the identification of intact protons from collisions, which is usually associated with elastic scattering of protons in the collision [20].

1.4.5 Muon spectrometer

The most outer part of the ATLAS detector is the Muon Spectrometer detecting charged particles in the region $\eta < 2.7$. The aim of the Muon spectrometer is to detect muons and measure their momenta. Muons are except neutrinos only particles escaping calorimeters. Hence there is the outer layer for better measurement of their properties to ensure a more precise understanding of collisions. The Muon spectrometer is made up of four parts with slightly

different purposes or technology used. These segments are displayed in Fig. 1.14:

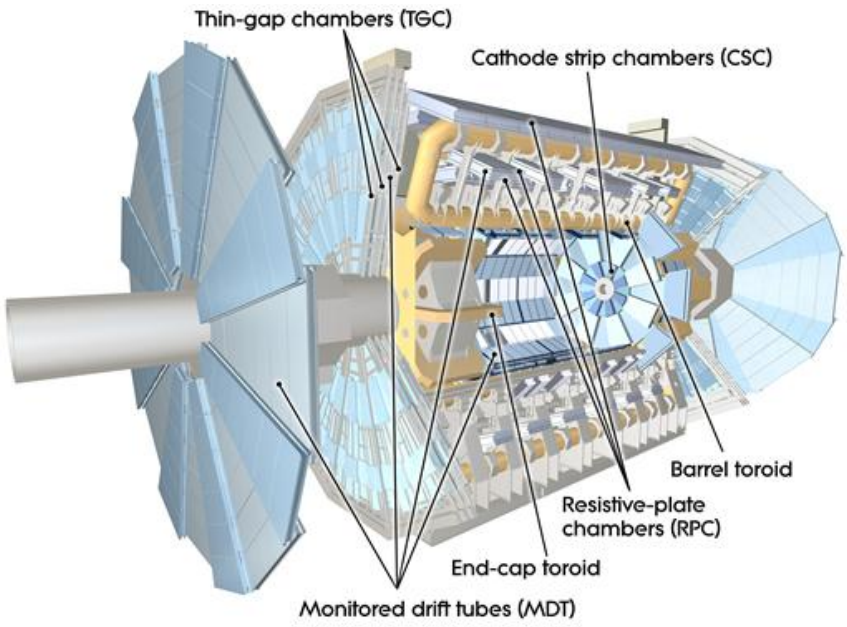

Figure 1.14: Schematic image of the ATLAS Muons system with titles of individual sub-systems. [21]

The Monitored drift tubes (MDT) and Cathode strip chambers (CSC) are detectors measuring the position of the muon to provide information to calculate the particle's momentum. The Thin-gap chambers (TGC) and Resistive-plate chambers (RPC) are used in the trigger system. The information allows recognition of a multiplicity of tracks and approximate energy ranges. Trigger chambers, as the two last are called, also provide robustness to hits from radiation background in the experimental hall [15].

The Resistive-plate chambers, located in the detector's barrel section, consist of three concentric cylindrical layers. The outer layer is used for triggering high momentum tracks ($9-35\,\mathrm{GeV}$), and the inner two layers are for low momentum ($6-9\,\mathrm{GeV}$). The RPC are parallel electrode plates 2 mm from each other without any wire. An electric field about $4.9\,\mathrm{kV{\cdot}mm^{-1}}$ between plates allows particles flying through the plates to generate avalanches along the track. The signal is read out to a metallic strip using capacitive coupling [15].

Thin-gap chambers provide information mostly about false coincidence hits from radiation background in the end-cap region; hence, most background radiation comes from the beam line sector. To ensure that seven layers of TGC are located in the end-cap region. The second function of TGC is the determination of the azimuthal coordinate, which is a complement to the measurement from MDT. TGC is a multi-wire proportional chamber with graphite layers, where a gas mixture of CO_2 and n-pentane with wires are between them.

The MDT consists of more than three hundred thousand tubes with 29.97 mm in diameter filed with a gas mixture of Ar and CO_2 (93/7) operating in the pressure 3 bar. The charge from ionization created by charge particles flying

through the detector is collected at the tungsten-rhenium wire at the center of the tube.

Cathode strip chambers are used in the region $2 < \eta < 2.7$ where MDT can not provide satisfying results due to higher particle densities in this region. CSC is also suitable for lower neutron sensitivity of used gas in the chambers.

1.4.6 Trigger system

A trigger system is used to avoid saving large amounts of data without processes of particular interest. Thus triggers select only those events which are physic important by set criteria.

The ATLAS trigger system consists of two sub-systems, level-1 (L1) and high-level trigger (HLT). The L1 trigger is made up of custom-made electronics to ensure a read-out accept rate satisfies the frequency of collision of about 1 billion per second. For the reason of such high frequency, the initial part of the L1 trigger decision is done by a logical hardware component placed typically near sensors just behind the read-out electronics. [15]. The rate of up to 100 kHz selected by the L1 trigger is passed to HLT for further processing. The main sub-systems of the L1 trigger are in the Muon spectrometer and calorimeters, shown in the schematic diagram in Fig. 1.15.

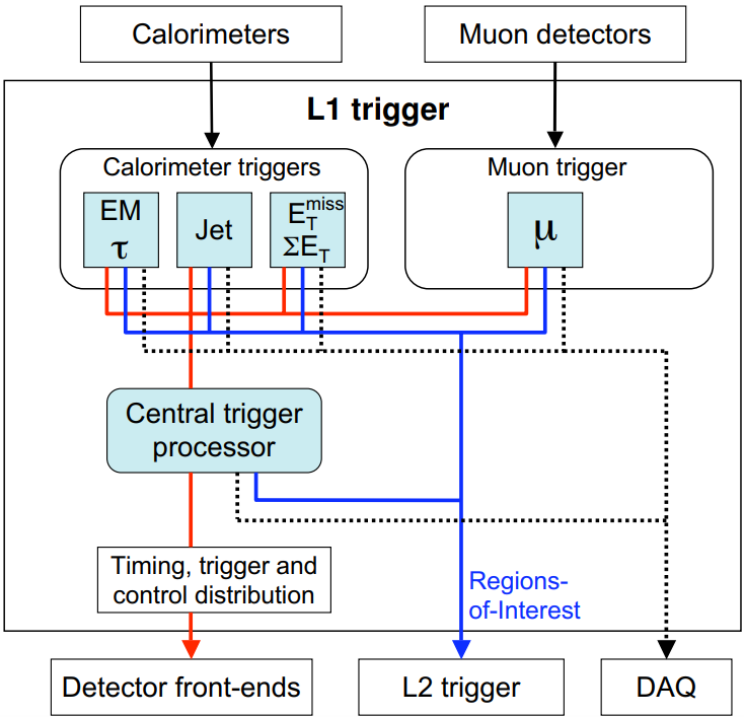

Figure 1.15: Diagram of the L1 trigger system working. [15]

Heavy ion collisions at ATLAS have different properties concerning the trigger system, such as the rate of the collisions (48 kHz - hadronic interactions and 1.5 MHz - single *PbPb* electromagnetic dissociation [22]) and size of the events (5 Mb, in the case of *pp* 1.5 Mb) [23].

L1 triggers in HI collisions select events containing jets, photons, electrons, and muons. A specific set of triggers to select ultra-peripheral events are used.

The events from L1 are sent to HLT for further processing. HLT is a software base trigger operating similar algorithms and is used in offline reconstructions. HLT thus improves on L1 decision and can also select various event topologies. A large rate of minimum-bias events is also recorded. The typical event recording rate is about 1.5 kHz.

2. Physics Background

All physics used in this field is based on quantum mechanics and quantum field theory. We will cover only the basics of principles and some naive intuitive imagination of the problems. We recommend checking other sources for a better understanding.

2.1 The Standard Model of Particle Physics

Physical processes in particle collisions are well described by the set of theories called The Standard Model of Particle Physics (SM). Except for gravity, the other three fundamental interactions are covered in SM. In this theory, all known elementary particles are classified into fermions, such as quarks and leptons, and bosons, such as interaction carriers and Higgs boson. All particles and their approximate basic properties can be seen in the picture in Fig. 2.1 All

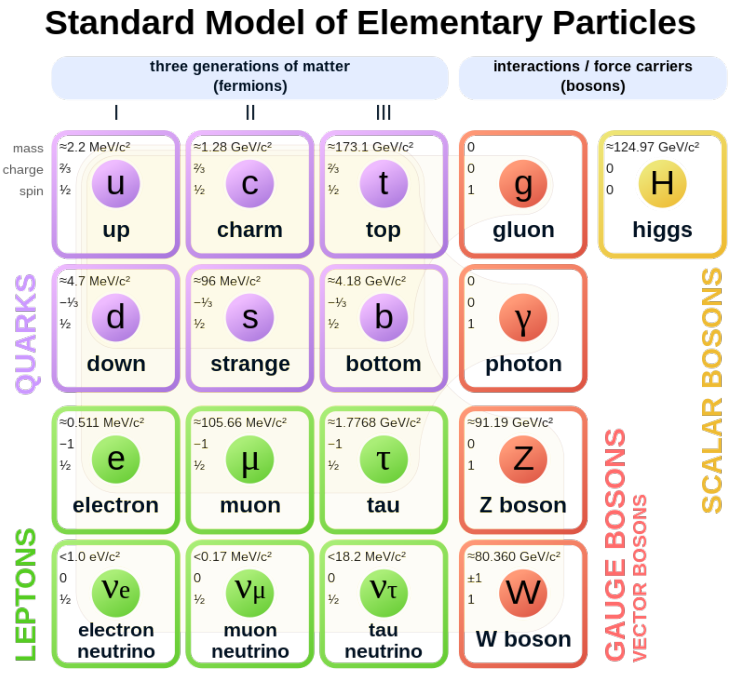

Figure 2.1: Table of particles in the Standard Model of Particle Physics. [24]

the particles have their anti-particles with the same mass but opposite quantum physical charges. Quarks make up composed particles named hadrons which can be divided into two groups. Mesons, which are made from an equal number of quarks and anti-quarks, and baryons, which are made up of an odd number of quarks. All matter that humans can usually witness is made up of u and d quarks and electrons.

Electroweak bosons Z and W are important for our topic. The reason is that the electroweak bosons do not interact via strong force but have significant decay channels into quarks. That makes them possible candidates to probe quark-gluon

plasma, which is an environment opaque to particles interacting via the strong force. More about quark-gluon plasma (QGP) in the section 2.3.

2.1.1 Quantum Chromodynamics

Quantum chromodynamics (QCD) is currently the best theory describing the strong force. In contrast with quantum electrodynamics (QED), where electromagnetic force has two possible elementary charges, the QCD has three charges named after colors: red, blue, and green. Another significant difference is in the particle carrying the force, gluon. Photon has no electric charge in contrast with gluon, which has a color charge. That is one of the reasons why QCD is more complicated and non-intuitive.

Quarks are binded together by exchanging gluons between them. The farther quarks are from each other stronger the force binding them together is. This behavior leads to properties determining why color-charged particles are not observed alone in nature. Bound states of quarks have a size in which quarks bearly interact with each other; this condition is called asymptotic freedom. As mentioned above, hadrons from the outside can be described as the composite state of quarks. From inside, hadrons are a much more complicated structure of quarks, gluons, and constantly created pairs of quarks and anti-quarks. Everything that could be part of hadrons is summarily called partons [1]. Partons creating externally observable properties of the hadron are called valence quarks, in contrast with other's so-called sea quarks. At any time, partons in the hadron interact with each other hence participants have a different fraction of the whole energy[2] of the system. Functions describing this fraction of individual partons are called the Parton distribution functions (PDF). They depend on the momentum transfer Q between partons. For example, the proton comprises two *up* and one *down* valence quarks, and its PDF can be seen in the picture in Fig. 2.2.

[1] from words "PARts of the proTON"

[2] In fact, in PDF, fractions of four-momenta of parton and the proton are used.

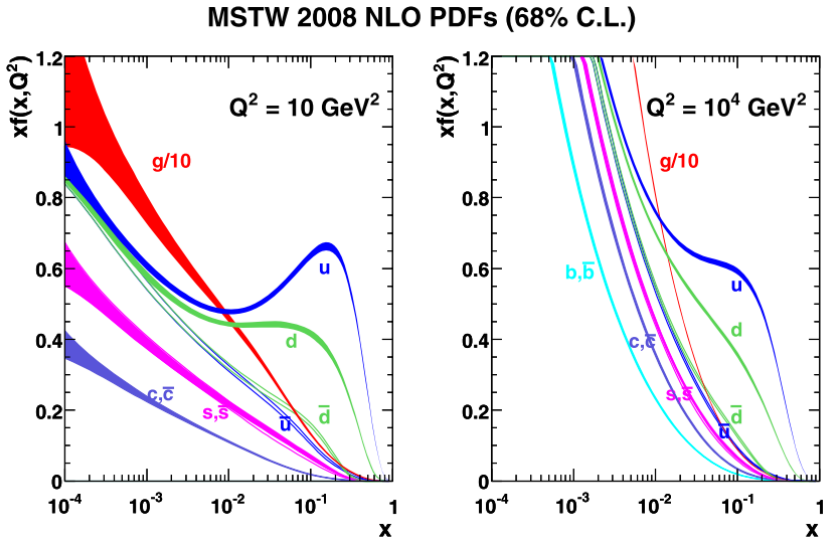

Figure 2.2: Parton distribution functions relevant at LHC energies with two different Q momentum transfer in the proton-proton collision. Dependences of probability density on the fraction x of energy of parton to the energy of the proton. [25]

2.2 Heavy Ions collisions

At the LHC, most of the time, protons collide with other protons. This collision is often called *pp* collision. In every collision of two bunches, multiple proton pairs have been collided. Nevertheless, in every collision, individual partons have collided with some momentum given by PDFs.

Part of the year, heavy ions (HI) collisions are studied for a better understanding of different processes and more complex phenomena, which we will discuss in chapter 2.3. At LHC, ions of Xe and Pb have been collided in the last few years. The section discussing the geometry of HI collisions is inspired by [26] based on the Glaber model. Everything we know a priori about the colliding system are nuclei which we collide together, and the energy of the nuclei. In contrast with *pp* collisions, where indeterminate factors represent PDFs alone, the heavy ions collisions have other factors playing a role in the problem. First of all, the centrality of the collision, which is very often described by impact parameter b. The impact parameter is defined as the transverse distance between the center of masses of both nuclei. However, the impact factor can not be measured experimentally, and different variables are used to define the centrality of the collision. The centrality of the collision can be estimated from energy deposited in forward calorimeters (FCal, ZDC). Second, the PDF of the nucleon bounded in the nuclei is different with respect to the one in the vacuum. This is usually referred to as nPDF and leads to so-called cold nuclear effects [27]. In nuclear physics are well approximative models for nucleon momenta distribution, and for individual nucleons, we can use PDFs for protons and neutrons. Let us assume N_A number of nucleons in nuclei A, then HI collision can be imagined[3] as a collision of N_A spheres with

[3]Based on Glabuer model.

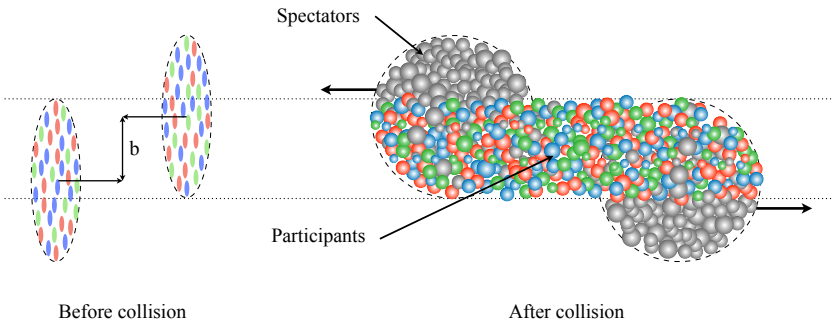

Figure 2.3: A computer generated schema of a heavy-ion collision. The impact parameter b is shown as well as the spectator and participant nucleons.[28].

radius r_n defined as:

$$r_n = \sqrt{\frac{\sigma_{pp}}{4\pi}}\,, \tag{2.1}$$

where σ_{pp} is cross-section of pp collision. Dimensions of HI are not spherical from the laboratory view due to the Lorentz factor. Let's denote ${r_A}^4$ as the stationary radius of the nucleus, then in LHC longitudinal dimension of the nucleus is $2r_A/\gamma$, where γ is the Lorentz factor (in run 2 in LHC, $\gamma \approx 2\,600$ for $\sqrt{s_{NN}} = 5.02\,\text{TeV}$). Considering the momentum of HI in LHC, ions can be imagined as thin disks (almost as 2D objects). Nevertheless, in the center of ions, there are more nucleons than at the edge, based on geometric properties. Hence nucleons from one nucleus have more other nucleons on their way through the second nucleus if they fly through the center of the nucleus than at the edge. Let us have two participant nuclei, A and B. Then we denote $N_{\text{part}} + N_{\text{spec}} = N_A + N_B$ and N_{coll} as the number of nucleon-nucleon collisions, where N_{part} is the number of nucleons participating in the collisions and N_{spec} number of spectator, non-interaction, nucleons. In an actual central HI collision, the nucleon in the center of A hits about 12 nucleons[5] from B. That means that N_{coll} could be much higher than N_{part}, especially in central collisions.

From studied colorless particles like γ and Z^0 in pp and HI collisions [30, 31], we can assume a good understanding of the initial hard interaction and collision geometry in HI collisions, at least in high p_{T} . On the other hand, measurement of colored probes like jets shows significant differences from pp collisions, proving a new state of matter, Quark-Gluon plasma (QGP). Some manifestations (the azimuthal anisotropies, for example) of this exotic state of matter have been observed in other collisions as pA (proton-ion) or even in pp. Still, some remain exclusive for heavy-ion collisions (for example, jet quenching, more in chapter 2.3.3). The existence of QGP in other than HI collisions has yet to be well known.

[4]The charge radius of the lead nucleus is approximately 5.5 fm [29]

[5]The collision nucleon-nucleon does not mean the destruction of the nucleon. Based on PDFs, only one pair of partons interacts (statistically).

2.3 Quark-gluon plasma

In the collision of HI, up to 30 thousand particles were created, which leads to an enormous increase of entropy [26]. Energy density in typical hadrons is about $500\,\mathrm{MeV/fm^3}$. A rough estimate of energy density in the $PbPb$ collision with $\sqrt{s_{NN}} = 2.76\,\mathrm{TeV}$ is about $12\,\mathrm{GeV/fm^3}$. Calculations of QCD thermodynamics show the theoretical state of matter in equilibrium at a temperature of about 300 MeV, which has an energy density $12.7\,\mathrm{GeV/fm^3}$. Energy density in the head-head HI collisions is more than 20 times larger than in typical hadrons. Thus color particles produced in the HI collision are in a different state of matter than classical Hadronic matter or Hadronic Gas. Quarks and gluons form a strongly color-coupled medium that behaves as a relativistic hydrodynamic fluid, called Quark-Gluon plasma (QGP) [26]. The phase diagram of QGP is in Fig. 2.4.

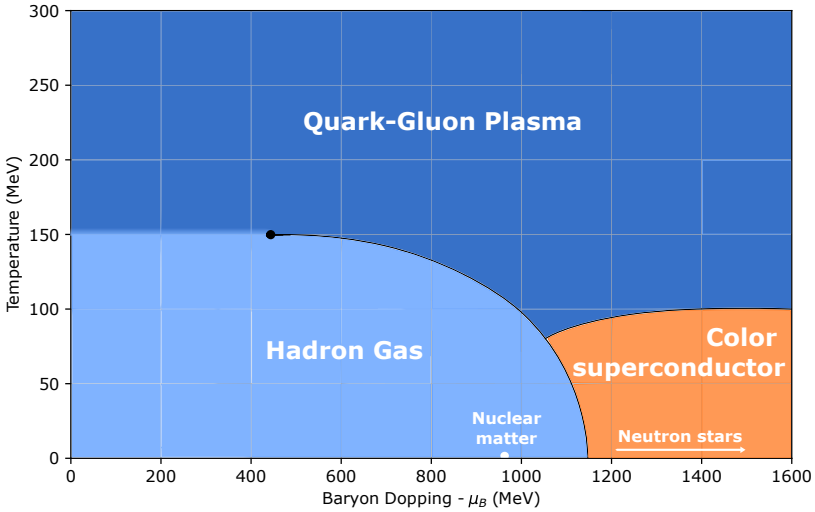

Figure 2.4: Phase diagram of Quark-Gluon Plasma. Baryon dopping μ_B is an excess of quarks over anti-quarks parametrized by chemical potential. Own creation, inspired from [26].

2.3.1 Glauber model of QGP

There exist microscopic models of QGP working on the principle of superposition pp collision with free parameters to model QGP. We will not talk about them and will focus on hydrodynamic models. The description of the geometry of HI collision, as it is mentioned in chapter 2.3, is based on the Glauber model, and we will discuss it more.

Observed properties of QGP described in the chapter above could be well explained by relativistic hydrodynamics of fluid, which expands and flows radially at about half the speed of light [26]. In the model, QGP as a fluid has low viscosity to entropy ratio $\eta/s = \frac{\pi}{4}$ (in units $\hbar = k_b = 1$), the lowest of known fluids. The hydrodynamic point of view explains azimuthal anisotropy in the following. In the first approximation, the initial geometry of collision has an elliptic form. In the second approximation, the nuclei are not homogeneous

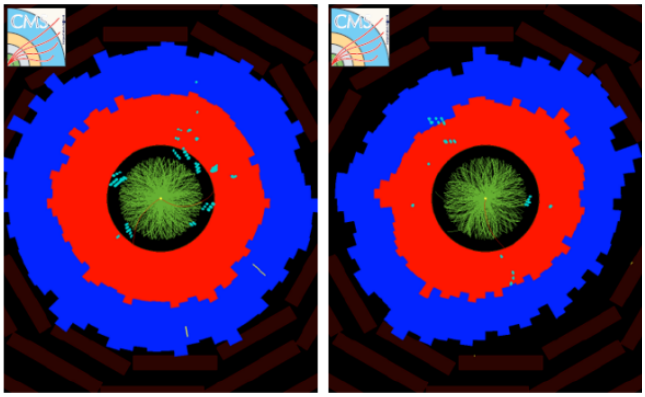

Figure 2.5: HI collision from CMS detector. Green lines in the picture show tracks of charged particles, and red and blue areas display measured energy in the electromagnetic and hadronic calorimeters, respectively. Azimuthal anisotropy in the energy flow appears on the right. [26].

structures; they have regions of higher densities, nucleons. That means in the first moment after the collision, the energy density of the matter must be lumpy too. If gas-like plasma were created, particles barely interact with each other, and discrepancies in density would disappear very quickly as particles fly in random directions. In contrast, lumpy parts in the fluid form of matter as well as the elliptic geometry, create pressure gradients that drive anisotropic flows in the fluid. We see azimuthal anisotropy of particles in the final state, which leads to an assumption that QGP is fluid with very low viscosity. Contrariwise, if the fluid's viscosity is high, flows would be damp out.

The temperature of the QGP is highly dependent on the position. In the center of the QGP is a higher temperature than at the edge of the plasma. It turns out from HYDJET++ Monte Carlo simulation published recently [32] that the centrality of the collision affects the temperature of QGP and p_{T} suppression[6].

2.3.2 Flow and space-time evolution

One of the descriptions of evolution in HI collision is proposed in [33] by Bjorken in 1983. We came from this point of view with some more recent information from [26] about QGP. As we described in the chapter about HI collisions 2.2, in the Glaber model, nuclei move in straight lines and pass through each other. Over a brief period, N_{coll} of interactions occurred between nucleons, creating lumpy matter. After a not-yet-known period of time, by some models approximated to $\tau_{\mathrm{hydro}} \sim 0.7/T_{\mathrm{hydro}}$[7], matter hydrodynamize to a relativistic liquid of deconfined quarks and gluons with very low viscosity. More complex simulation [34] of QGP leads to number $\tau_{\mathrm{hydro}} \approx 0.35\,\mathrm{fm/c}$. Shortly after that, the thermal equilibrium in QGP is established in temperature about 300 MeV. The hydrodynamic nature of the QGP converts spatial anisotropies into momentum anisotropies. Flows of the fluid lead to future perturbation of particle azimuthal distribution. As the fluid expands, it cools. At the moment,

[6]particle with color losing energy as it moves through the QGP. More about it in the case of jets is provided in chapter 2.3.3.

[7]Where $T_{\mathrm{hydro}} \approx 560\,\mathrm{MeV}$ is the temperature of hydrodynamization of matter.

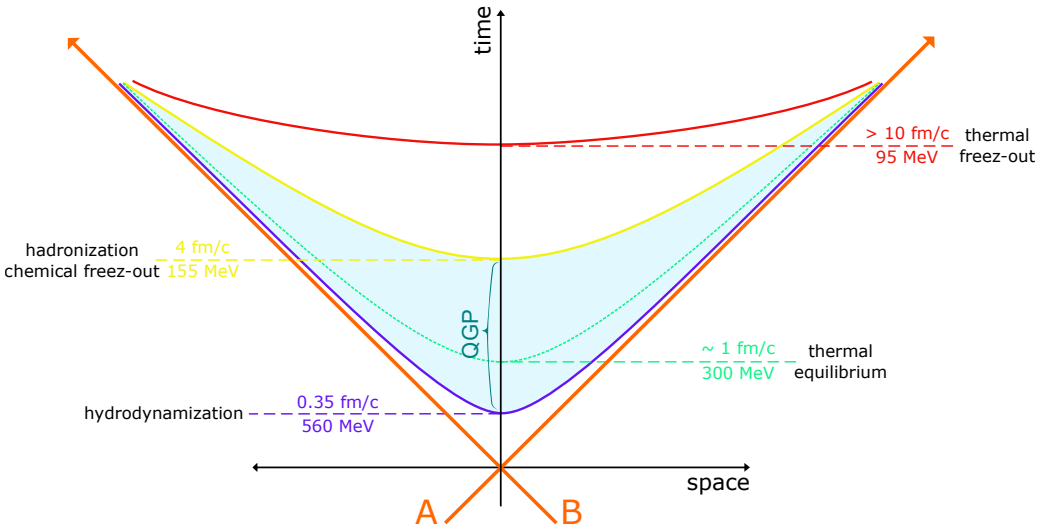

Figure 2.6: Space-time diagram of the evolution of the QGP with captions of individual stages. Proper time and temperature are inscribed in the picture (for $PbPb$ in LHC with $\sqrt{s_{NN}} = 5.02\,\mathrm{TeV}$).

when the temperature falls below $T_{\mathrm{QGP}} = 155\,\mathrm{MeV}$[8], the QGP goes through a phase transition and starts to hadronize. That is called chemical freeze-out, and it happens after a few fm/c. In the hadronization process, free quarks and gluons are formed into hadrons. Expanding clumps of hadrons interacting with each other until they are too far apiece, equivalent to a temperature of about 95 MeV. This is called thermal freeze-out. For further discussion, the time dimensions of the QGP lifespan will be important. Let us rewrite the times of individual stages of QGP described above in more imaginable units in the table 2.1:

	note	time [fm/c]	time [s]
collision time	$2r_A/\gamma$	**0.002**	$\mathbf{7 \cdot 10^{-27}}$
thermalization time		**0.35**	$\mathbf{1.2 \cdot 10^{-24}}$
hadronization time		a few	$\mathbf{10^{-23}}$

Table 2.1: Table of the time evolution of QGP stages.

2.3.3 Jets and Jet quenching

As we discuss in chapter 2.1.1, quarks are bound tighter together as they move from apart. Energy in the bond increases until it is so much that it creates new pair of quarks (quark and anti-quark). It can be imagined as pulling the string. When it rips, it releases energy and creates new particles. This phenomenon is called hadronization. If the initial parton has enough energy, this process continues, creating more hadrons. The initial parton has high momentum. Hence all created particles are collimated in a cone. The shower of these hadrons is called a jet. Jets are typically created in hard scattering - an inelastic collision of two partons with high momentum transfer or in the decay of massive particles.

[8] T_{QGP} vary according to baryon doping, see Fig. 2.4.

Lots of hadrons created in the shower have no long lifetime and would decay before they reach the detector. Products of these decays move along the rest of the initial jet and are considered as part of it in the detector.

Jet, by definition, comes from color particles. Hence their properties depend on the Quark-gluon plasma as the constituents fly through the fluid. QGP-induced modification of the jet is called jet quenching. The name of the phenomenon came from the direct consequence of the energy loss of parton in QGP, which is the reduction of energy of the jet and modification to the jet fragmentation functions. The main energy loss mechanism for highly energetic partons is gluon radiation induced by QGP [35]. For the reason of calculation, mainly two limiting approximations of gluon radiation are considered.

- Interaction with the medium is via only a few hard scattering.
- Interaction with the medium is coherent, mediated by multiple soft scattering.

According to the position of the process in the QGP, which created the jets[9], one of the jets could be changed by jet quenching much more than the other. This phenomenon is shown in Fig. 2.7. The jet supression can be characterized by

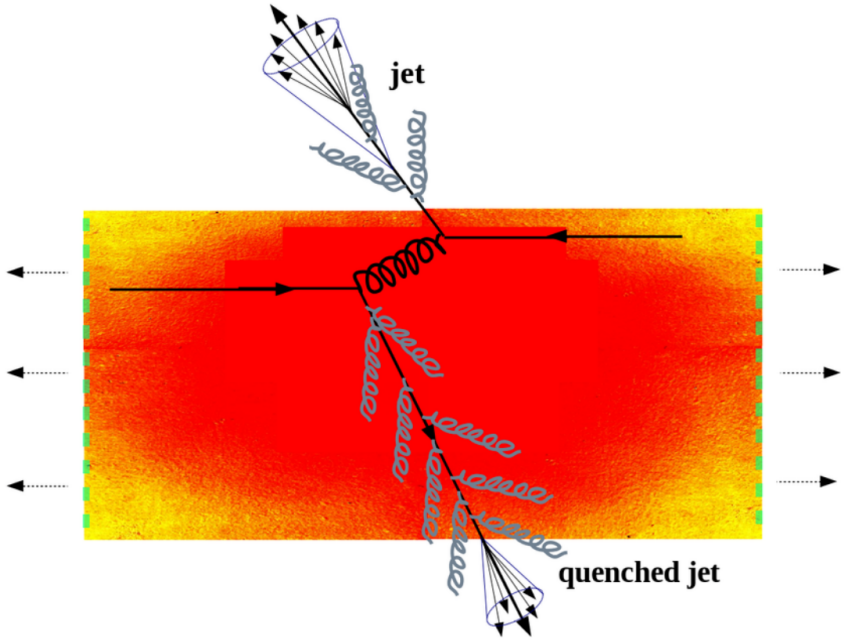

Figure 2.7: Illustration showing phenomenon of jet quenching. The bottom parton radiates gluons as it moves through the QGP, resulting in the final jet being quenched. [32]

R_{AA} the nuclear modification factor defined as [26]:

$$R_{AA}(p_{\mathrm{T}}) = \frac{dN^{AA}/dp_{\mathrm{T}}}{\langle N_{\mathrm{coll}} \rangle \, dN^{pp}/dp_{\mathrm{T}}} \,, \tag{2.2}$$

where dN^{xx}/dp_{T} are yields of jets in pp or AA collisions. The R_{AA} factor is used for the comparison of pp and HI collisions. If the behavior of jets was not affected

[9] Assuming pair of jets is created back-to-back in the azimuthal direction.

in QGP, the R_{AA} would be equal to one. That is not the case, R_{AA} was measured to be smaller than one [36], and the value depends on the p_{T} of the jet and on the centrality of the collision, which affect the size of the volume of QGP. The dependence of the R_{AA} on the p_{T} and centrality of the collision from measured data on LHC is shown in Fig. 2.8.

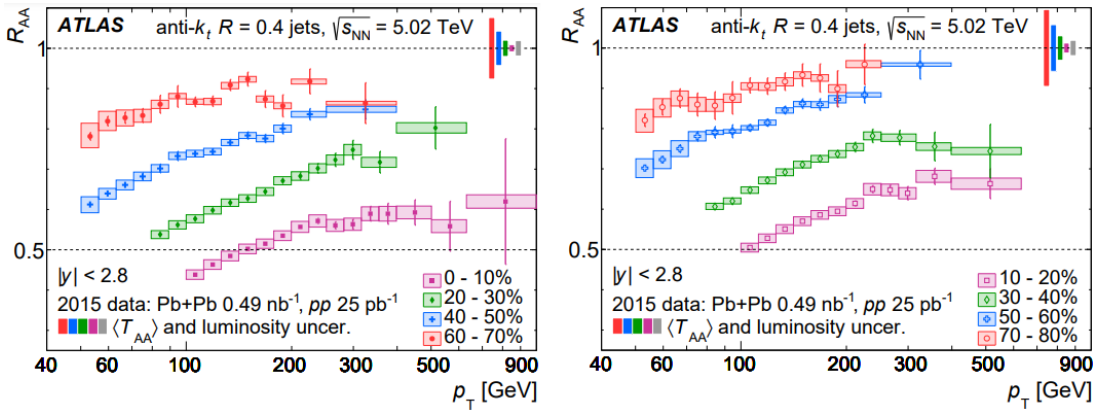

Figure 2.8: Graph of R_{AA} values as a function of p_{T} of jets with different centrality (distinguished by the color - legend). The error bars represent statistical uncertainties, and the colored boxes around the data points represent bin-wise correlated systematic uncertainties. [36]

2.3.4 Electroweak bosons as probes of QGP

Objects from hard scattering with high p_{T} could be used as probes for studying quark-gluon plasma. For that purpose, jets are often used as an object subjecting to quenching in the QGP. We can quantify the properties of the QGP by the measurement of the jets in the experiment with heavy-ions collisions. Determining the properties of QGP from measured quantities of jets is not trivial. Hence jet is often affected by multiple effects at once [35].

The electroweak bosons do not interact via the strong force. Thus they fly through the QGP almost unaffected. However, they dominantly decay to quarks, which are affected by QGP, and produced jets from this decay can be detected.

Particle	hadron channel [%]
W	67.4 ± 0.3
Z	69.91 ± 0.06

Table 2.2: Table of the percentage of hadron decay channel of electroweak bosons. [9]

The mean lifetime of a particle can be calculated by the following formula:

$$\tau = \frac{\hbar}{\Gamma}, \tag{2.3}$$

where Γ is the decay full width of the particle. The full width of the Z boson is $\Gamma = (2.495 \pm 0.002)$ GeV and of the W boson is $\Gamma = (2.085 \pm 0.042)$ GeV [9]. Thus

by applicating eq. (2.3) we get approximately for both bosons $\tau \approx 3 \cdot 10^{-25}\,\mathrm{s}$. Let us assume that most of the bosons have a maximum $p_T < 300\,\mathrm{GeV}$. The proper time of the particle in the laboratory system is $t' = \gamma t$. Then the mean lifetime of the maximum boosted electroweak boson would be:[10]

$$\tau' = \gamma\tau = \frac{E}{m_0 c^2}\tau; \qquad E^2 = (pc)^2 + (m_0 c^2)^2 \tag{2.4}$$

$$\implies c\tau'_W = 9.5 \cdot 10^{-17}\mathrm{m} \qquad \implies c\tau'_Z = 7.9 \cdot 10^{-17}\mathrm{m} \tag{2.5}$$

$$\implies \tau'_W = \frac{310.5}{80.4}\mathrm{GeV} \cdot 3.16 \cdot 10^{-25}\,\mathrm{s} = 1.23 \cdot 10^{-24}\,\mathrm{s}\,, \tag{2.6}$$

$$\implies \tau'_Z = \frac{313.5}{91.2}\mathrm{GeV} \cdot 2.64 \cdot 10^{-25}\,\mathrm{s} = 0.90 \cdot 10^{-24}\,\mathrm{s}\,. \tag{2.7}$$

Let us compare results from equations (2.6) and (2.7) with time scales in the tab. 2.1. We can safely say that even highly boosted electroweak bosons have minimal chance to survive through the whole evolution of QGP and decay after that. Thus all particles from the decay of these bosons would be present in the QGP. Comparing the reach of the bosons with the size of the lead nucleus and the typical size of the QGP (Tab. 2.1) results in 20 times shorter reach than the compared sizes.

Despite that very short lifetime, most of the bosons with lower momenta would decay before QGP thermalization. That results in no observation of the movement of bosons in QGP and potentialal difference in quenching of the two jets from boson decay depending on the boost of the boson. Let's calculate the needed p_T of the electroweak bosons, which leads to a substantially long lifetime, approximately $\tau' \approx 5.10 \cdot 10^{-24}\,\mathrm{s}$, which leads roughly to half of the lifetime of QGP ($PbPb$ with $\sqrt{s_{NN}} = 5.02\,\mathrm{TeV}$). Let us derive from eq. (2.4):

$$E = \frac{\tau'}{\tau} m_0 c^2$$

$$p_\mathrm{T}|_{min}{}^2 c^2 = \left(\frac{\tau'}{\tau}\right)^2 m_0{}^2 c^4 - (m_0 c^2)^2$$

$$p_\mathrm{T}|_{min}\, c = m_0 c^2 \sqrt{\left(\frac{\tau'}{\tau}\right)^2 - 1} \tag{2.8}$$

$$\implies p_\mathrm{T}|_{min-W} = 1266\,\mathrm{GeV} \tag{2.9}$$

$$\implies p_\mathrm{T}|_{min-Z} = 1725\,\mathrm{GeV}\,. \tag{2.10}$$

As we can see from results in equations (2.9) and (2.10), in the current LHC are no chance to probe the time evolution of QGP with W and Z bosons. In the future FCC (Future Circular Collider), it could be possible effectively observe the decay of electroweak bosons inside the volume of the QGP. Nevertheless, studying such processes of electroweak bosons is important in LHC. Thus, Jets from their decay is quark jets and could have different behavior in the QGP than the gluon jets.

Electroweak bosons, as we saw in the tab. 2.2, have dominant hadrons decay channel. After the decay of the boson, two jets could be observed in the detector

[10] In our calculation, we ignore the nontransversal component of momentum. We assumed maximum p_T for the case of $\eta = 0$ because our goal is a rough estimate. In the general case, we could specify the whole momentum.

with an angle θ between them. We can safely assume that jets would have high p_{T} . Let us derive from the law of conversation of four-momentum[11]

$$\begin{aligned} P_{ewb} &= P_1 + P_2 \\ {m_{ewb}}^2 &= (E_1 + E_2)^2 - ({p_1}^2 + 2p_1 p_2 \cos(\theta) + {p_2}^2)\,, \end{aligned} \tag{2.11}$$

where θ is the angle between two jets coming from the decay of the electroweak boson. Let us assume an angle between jets only in the transversal plane. Then the $p \implies p_{\mathrm{T}}$ and angle $\theta \implies d\phi$. Jets with high p_{T} are comprised of lots of hadrons with a mass much lower than their momentum. Thus we can approximate that $E_i = p_i$. Than

$$d\phi = \frac{\pi}{180} \arccos\left(1 - \frac{{m_{ewb}}^2}{2{p_{\mathrm{T}}}^{jet1}{p_{\mathrm{T}}}^{jet2}}\right) . \tag{2.12}$$

Let us assume that p_{T} of both jets are similar, which has the highest probability. Then we can plot equation 2.12 as a function of p_{T} of W or Z boson in Fig. 2.9:

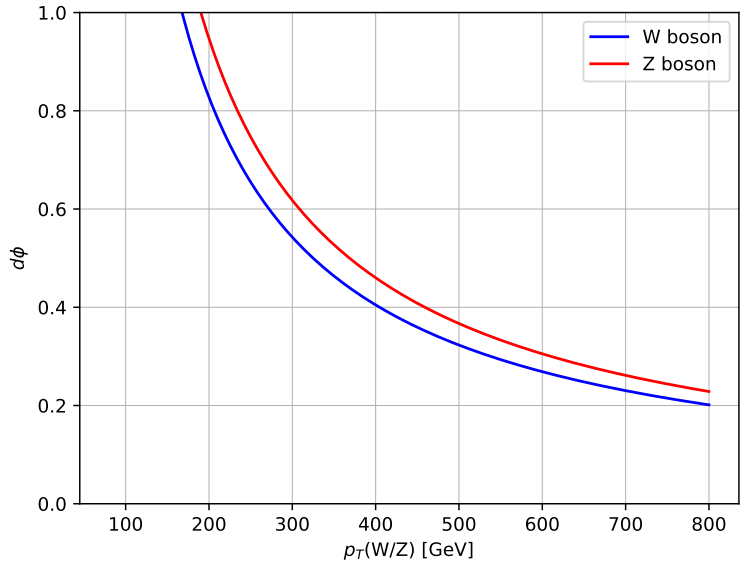

Figure 2.9: Graph of eq. 2.12 with the mass of Z and W bosons.

[11]In next calculations, we will use natural units, where $c = 1$.

3. Analysis procedure

3.1 Jets Reconstruction

In this chapter, we will first introduce the procedure of how we reconstruct jets. The procedure used here is generally different compared to what is used in experiments. Since we used the particle level simulations, we do not have to deal with the contribution from the backgrounds and with the jet calibration. In heavy-ion collisions, the calibration of the jets is slightly different than in the *pp* collisions. We do not discuss it here either. Conversely, we focus on the basics of jets reconstruction because different reconstructing jet algorithms are used in the next chapter 4. For more information, visit [35], which we are inspired from.

3.1.1 Jet parameters

The jet object has many different parameters additionally to p_{T}, ϕ, and other kinematic quantities as other particles. These parameters are later used to analyze data.

- **Jet radius - R** is the radius in which the jet is reconstructed from the hadrons. Is the same quantity as defined in the eq. 1.11 in the $\eta - \phi$ space.
- **R distance - $\mathbf{dR_{12}}$** is distance in $\eta - \phi$ space between two particles.
- **Splitting scale - $\sqrt{\mathbf{d_{12}}}$**, sometimes called k_T scale, is measured to classify splitting strength between two sub-jets. Indices 1 and 2 refer to prongs that were clustered last. It can also be defined with general tendencies i and j.
- $\sqrt{\mathbf{d_{iB}}}$ is the splitting scale between i-th particle and the beam.
- **Jet constituents** are all inputs to the jet clustering including particles, charged tracks, calorimetric towers, or clusters.

3.1.2 Cluster Algorithms

The jet clustering algorithm creates jets from many observed objects in the detector. Two main requirements for algorithms are infrared and collinear safety. The infrared safety (IRS) algorithm is resistant to the addition of low-momentum particles. If the algorithm is not IRS, then after adding a soft particle, the initial jet could be clustered with other particles which are close to the soft particle but normally will not be counted to the jet. For example, two jets could be clustered together if, in a non-IRS algorithm, a soft particle is added between them. Algorithms could also falsely identify one particle as two collinear particles and create two jets instead of one. For example, that could happen when the particle delivers energy between two cells in the calorimeter. The collinear safety (CLS) algorithm is immune to such a process.

Old non-safety cone algorithms used so-called seeds, highly energetic particles, as starting points from which they reconstructed the jet in the cone. One of the current infrared and collinear safety algorithms is a seedless SISCone algorithm.

The second type of algorithms is the Sequential Clustering Algorithms. In this type of algorithm, d_{ij} is used to determine the distance of the particles and determine which of them cluster to the jet. Particles with the smallest distant d_{ij} are clustered together first, then next by next, particles by the size of d_{ij} are added to the cluster gradually. The process is ended when the d_{iB} is smaller than the distance of the next particle. We consider two main Sequential Clustering Algorithms:

- **$\mathbf{k_T}$ algorithm** where is defined

$$d_{ij}^{k_T} = min(p_{\mathrm{T},i}^2, p_{\mathrm{T},j}^2)\frac{\Delta R_{ij}^2}{R^2}\,, \qquad d_{iB}^{k_T} = p_{\mathrm{T},i}^2\,. \tag{3.1}$$

  k_T algorithm function is, in principle, like inverse hadronization. The last prongs clustered are sub-jets from the most energetic first particles that were split from the initial parton. That is very convenient for the analysis of data because the clustering steps follow the time evolution of the parton shower.

- **Anti-$\mathbf{k_T}$ algorithm** where is defined [35]

$$d_{ij}^{\mathrm{anti}-k_T} = min\left(\frac{1}{p_{\mathrm{T},1}^2}, \frac{1}{p_{\mathrm{T},2}^2}\right)\frac{\Delta R_{ij}^2}{R^2}\,, \qquad d_{iB}^{\mathrm{anti}-k_T} = \frac{1}{p_{\mathrm{T},1}^2}\,. \tag{3.2}$$

  Anti-k_T algorithm is a fast and effective algorithm that's jet boundaries are resilient to soft radiation. Nevertheless, the separation of the jet into subjets is not physic justified. Hence the process of the clustering is opposite from the k_T algorithm.

Particles clustered to the jets by different algorithms lead to different results, which can be seen in Fig. 3.1. While it might seems that the k_T algorithm would be a better choice for the reasons mentioned above, experiments usually use the anti-k_T algorithm since that is much more robust against various backgrounds and contributions from underlying events.

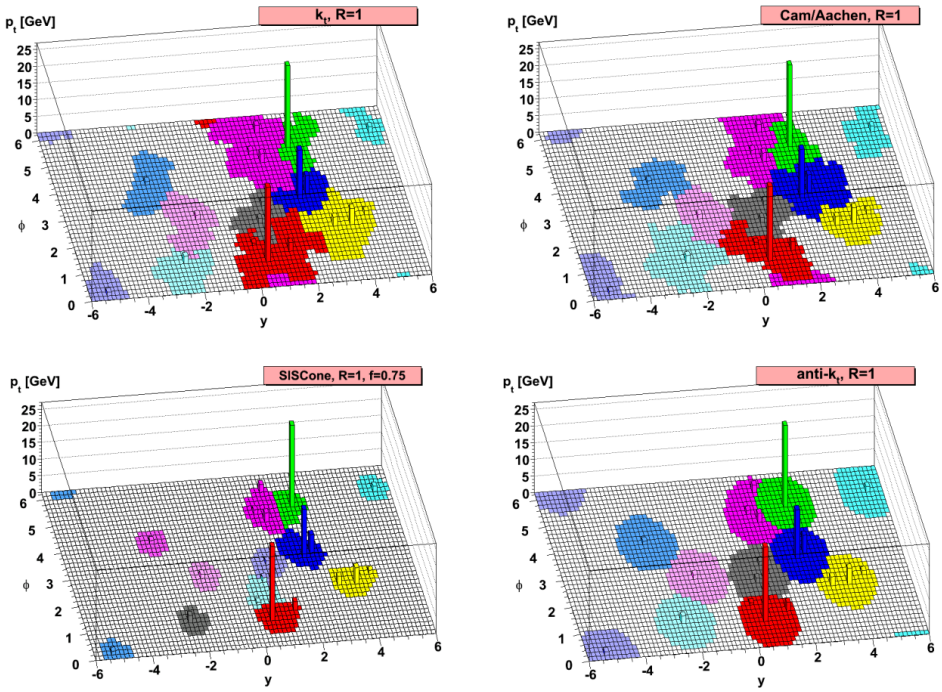

Figure 3.1: Comparison of jets reconstruction algorithms. [37]

3.2 Pythia 8

Pythia 8[1] is a software designed to simulate collisions of particles in particle physics [38]. It is compatible with CERN framework ROOT. Working with Pythia is accomplished in the C++ programming language, where it is included as a package. Pythia has lots of options. Our settings used to generate data analyzed in chapter 4 are shown in the appendix 4.3. We used two data samples, all hard QCD (let's label it QCD sample), to obtain inclusive jet samples. The second sample included processes with the production of W and Z bosons, which is our part of interest (let's label it EWB sample as ElectroWeak Bosons). For both types of samples, we generate simulation for three beam energy $\sqrt{s_{NN}} = 5.02\,\text{TeV}$ as a current value, $\sqrt{s_{NN}} = 5.36\,\text{TeV}$ as an upcoming value in the run 3 and $\sqrt{s_{NN}} = 5.50\,\text{TeV}$ as the potential future value. Each of the six samples is generated in four p_T intervals and merged together in the end. Values of the p_T intervals and a number of events are written in Tab. 3.1. Thus, the total number of generated events per sample is 20 million.

interval p_T [GeV]	Number of events
20-60	5 000 000
60-160	5 000 000
160-360	5 000 000
360-800	5 000 000

Table 3.1: Intervals of p_T in which we generate simulations with the number of events.

[1]We use version Pythia 8.303.

The generation of events in Pythia is done by Monte Carlo Method (MC simulations). The method is based on repeated random sampling [39]. The MC simulation is often used in probability deterministic situations such as processes of QCD and QED in the case of particle collisions.

Pythia generates event-by-event. In our case, we generated pp collisions with the kinematics of $PbPb$ collisions to study only the hard processes. In every event, there is a list of particles with properties. There is an example of properties that we will use:

- **Number in the event record** is the reference number of particles in the event.
- **particle ID** refers to the type of particle, for example, u quark or electron. The database of the ID codes is in [9] on page 560.
- **Status** code which tells in which phase of collision the particle is[2]. The details can be found in [40].
- **Mothers** and **Daughters** are referencing numbers to the Event number from which that particle is coming from (Mother) or which particles are created by decay or other interaction from that particle (Daughters).
- **Momenta** of the particles in different directions.
- **Angles ϕ, η** in which particles coming from the collision.

Pythia generates events gradually and propagates particles through different stages of the collision. Thus the same particle appears multiple times in the event tree[3] with different status codes as the particle has different roles in the processes of the collisions.

[2]For example, 23 is a status code for outgoing particles from the hardest subprocess

[3]Label for the list of all particles with event numbers.

4. Results

As we discuss in chapter 3.2, we generated four separate simulation samples for different p_{T} intervals and then merged them together. In merging, a total cross-section of the sample as well as the number of events was used as a weight to ensure the right normalization of values to cross-section σ of simulated dependencies. The results are reported as double or triple differential cross-sections in the multidimensional space of physical quantities. In all cases[1], we normalize σ to an interval of ϕ angle, which is equivalent to factor $1/2\pi$, and to the unit rapidity. Then we used normalization to other quantities according to a given case.

To cluster jets, we used the anti-k$_T$ algorithm with $R = 0.2$ that clusters all stable, final-state particle particles generated in Pythia with the exclusion of muons. On these jets, we apply cuts written down in Tab. 4.1, and the distributions of the number of these jets in the events are shown in Fig. 4.1. The figure compares the distributions in EWB and QCD samples.

Type of cut	value
p_{T}	$> 30\,\mathrm{GeV}$
$\lvert\eta\rvert$	< 3

Table 4.1: Table of cuts for $R = 0.2$ jets.

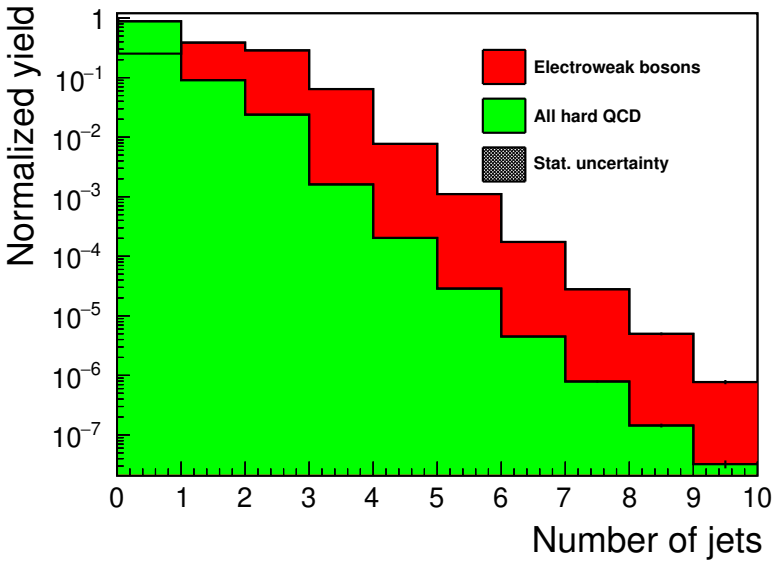

Figure 4.1: Per-event normalized distribution of the number of jets in the event compared in two samples, QCD (green) and EWB (red).

[1]Because we don't assume azimuthal anisotropy.

4.1 Jet re-clustering with R=1.0

Clustered $R = 0.2$ jets could be used again as input to the clustering algorithm for constructing larger jets. We will focus on that case because EWB could decay to quarks forming two jets. If that EWB is of high pT, the large $R = 1.0$ jet carries the whole available information about the EWB. This is a way how to enhance the signal with reference to QCD background. In the second clustering, we used the anti-k$_T$ algorithm with $R = 1.0$ with the same cust as for the $R = 0.2$ jets. In figure 4.2, there is p_{T} spectrum of small $R = 0.2$ jets and large $R = 1.0$ jets, from which it could be seen that difference between them is higher with increasing p_{T} (the larger difference is seen in the case of EWB than QCD sample as well, see Fig. 4.3). Remarkable differences between $R = 0.2$ and $R = 1.0$ jets in

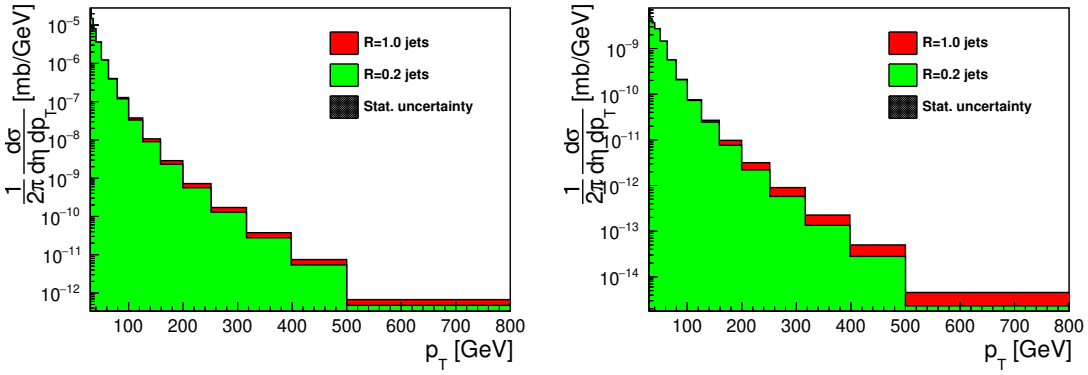

Figure 4.2: Jet cross-section of p_{T} for R=0.2 and R=1.0 jets from QCD sample (left) and EWB sample (right).

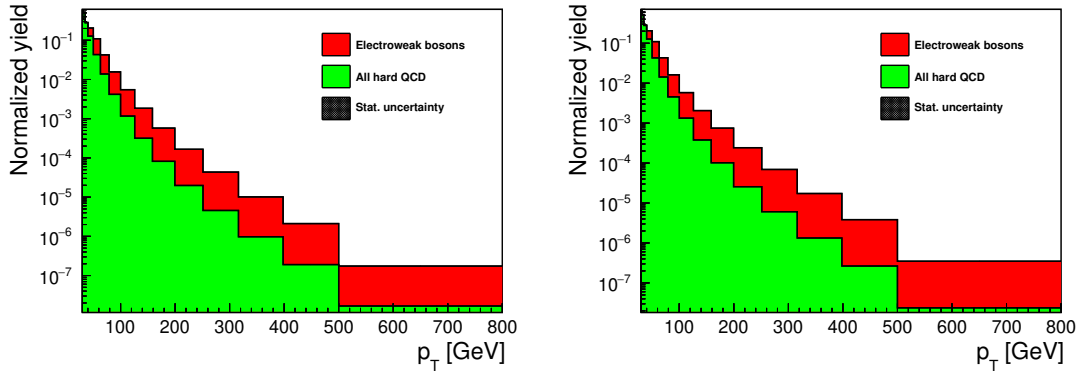

Figure 4.3: Per-event normalized p_{T} spectra of $R = 0.2$ jets (left) and large $R = 1.0$ jets (right) compared to with QCD sample (green) and EWB sample (red).

observed properties could be seen in their mass; see Fig. 4.4. As we can observe, a significant peak is visible in the region of EWB masses (for the right graph - EWB sample). Differences in the shape of the mass spectrum of the large $R = 1.0$ jets between samples of EWB and QCD could be seen better in the normalized Fig. 4.5. To get quantities describing the jet substructure, which could help in separating jets from EWB decays and QCD processes, we get jet constituents from large $R = 1.0$ jet and use them as an input to clustering again, but with the

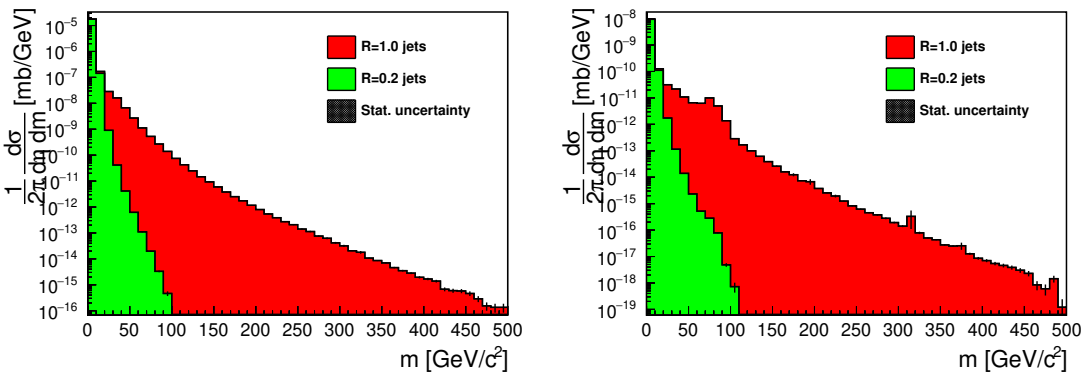

Figure 4.4: Jet cross-section as a function of the mass of $R = 0.2$ jets (green) and large $R = 1.0$ jets (red) compared to with QCD sample (left) and EWB sample (right).

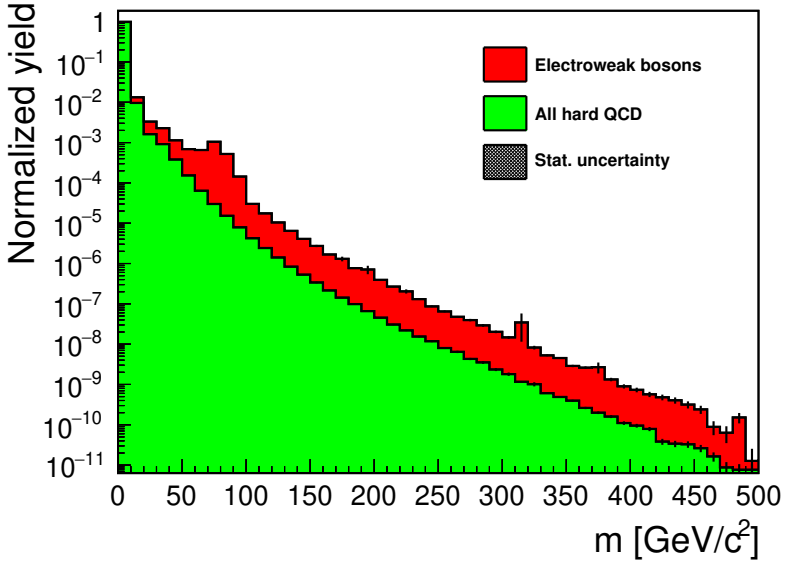

Figure 4.5: Per-event normalized distribution of mass of large $R = 1.0$ jets in QCD sample and EWB sample.

k_T algorithm. From such a constructed jet, we can compute variables $\sqrt{d_{12}}$ and dR_{12}, which can be seen in Fig. 4.6, where we compare these quantities between EWB and QCD sample. We can see from Fig. 4.6 that $\sqrt{d_{12}}$ is shifted towards higher in the case of electroweak bosons, which corresponded with imagination hard splitting of two quarks that have a similar momentum. That corresponds with the distribution of dR_{12}, which is also wider in the case of the EWB sample. Because the higher mass of particles that decay, the larger the angle between the products. Thus in the case of very massive EWB, cross-sections as a function of dR_{12} is also statistically larger than in the case of partons from the QCD sample.

Type of cut	value
p_{T}	$> 100\,\mathrm{GeV}$
$\lvert\eta\rvert$	< 3
# of subjets	≥ 2

Table 4.2: Table of cuts for $R = 1.0$ jets in the case of use for $\sqrt{d_{12}}$ or dR_{12}.

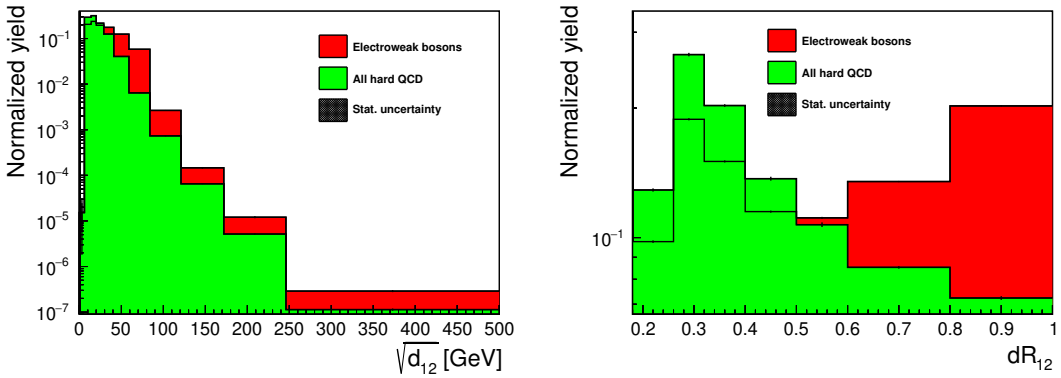

Figure 4.6: Per-event normalized distributions of larger $R = 1.0$ jets (re-clustered with k_T algorithm) as a function of $\sqrt{d_{12}}$ (left) and dR_{12} (right) in QCD sample (green) and EWB sample (RED).

We can draw two-dimensional histograms of $\sqrt{d_{12}}$ and dR_{12} depending on the p_{T} of the large jet, using cuts written in the tab. 4.2. In Fig. 4.7 in the top panel, we can see that $\sqrt{d_{12}}$ is correlated with p_{T} , for higher $\sqrt{d_{12}}$ the p_{T} of the large jet must be higher as well. In the lower histogram, we can see the signature of EWB in dR_{12} distribution, which we talk about more later in the next chapter 4.2.

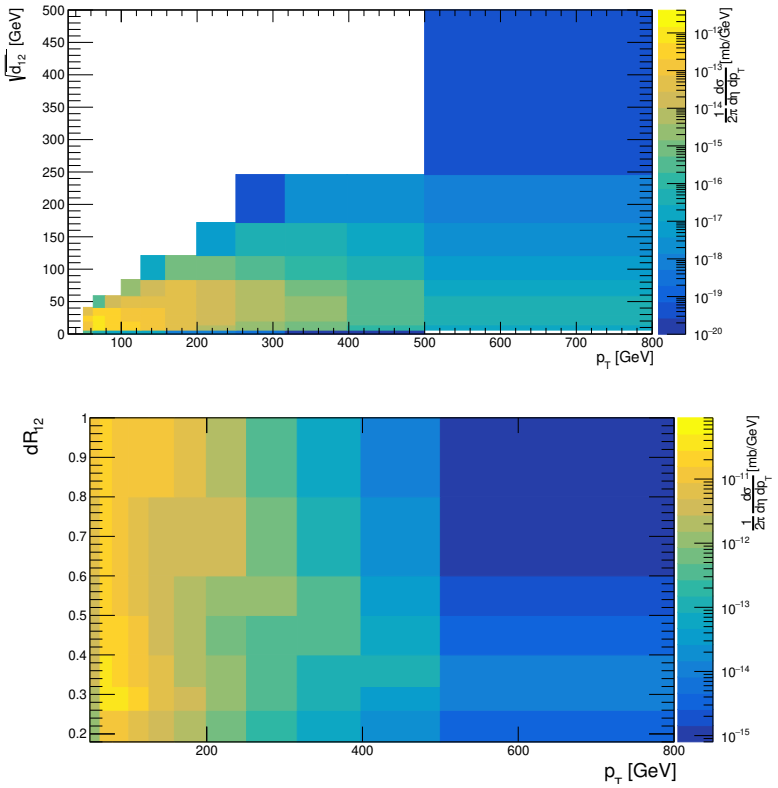

Figure 4.7: Dependence of $\sqrt{d_{12}}$ (top) and dR_{12} (bottom) on the p_{T} of large $R = 1.0$ (re-clustered with k_T algorithm). EWB sample is used.

4.2 Behavior of electroweak bosons

To get information from which primary particle (parton or EWB) the jet is coming, we use so-called tagging. It can be done only thanks to the information stored in the Pythia event since that is exclusive for simulation. In the first method of tagging (labeled: 1), we use the condition to the particle that it must be within the dR with the jet. In our case of large jets, we use the same dR as in the jet clustering, $dR = 1.0$. The second condition laid to the particles is their status. We use only particles with status code -23 (outgoing, not existing particles anymore - hard processes) or -62 (outgoing particles produced by the beam-remnant treatment, not existing anymore - for EWB). In case of multiple matches, the particle we tagged is that with the highest p_{T} . The second method uses re-clustered large jets with the k_T algorithm and undo the last clustering step into two sub-jets. For these sub-jets program uses the same system as mentioned above in method 1 (using $dR = 0.4$ for tagging). Then the program asked if the primary particles tagged to these sub-jets have the same *mother*. If so, the program save *mother's* ID as an ID of the tagged large jet. If not, then the zero is tagged as an ID, which does not correspond to any particle and can be easily identified later in the analysis. The difference between these two methods for jets above 30 GeV can be seen in Fig. 4.8, where the ID of tagged particles to large $R = 1.0$ jets is shown. The significant difference seen here is caused mainly by lower-pT jets with a single sub-jet that are tagged by method 1 but are not, by construction, tagged by method 2. From the distribution in

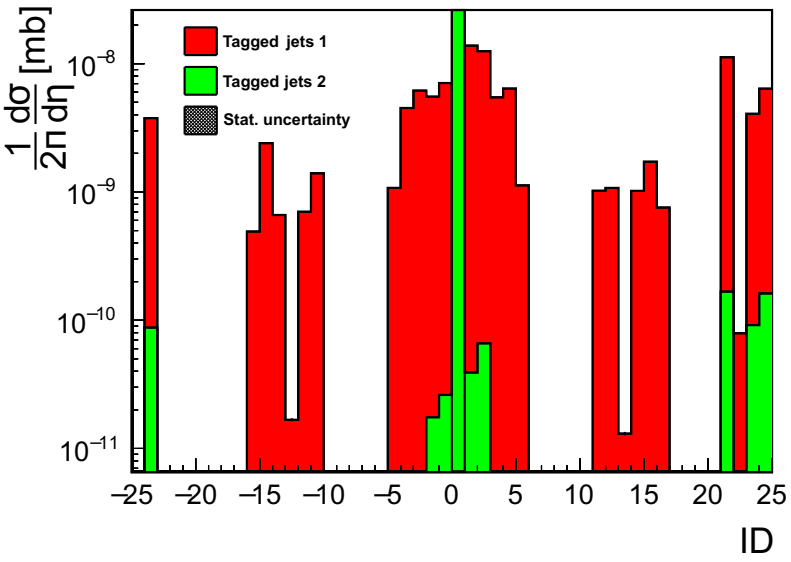

Figure 4.8: Comparison of distributions of ID tagged to larger $R = 1.0$ jets for two different tagging methods in EWB sample.

Fig. 4.9 showing the dR between the primary particle and the jet axis as a function of jet p_{T} , we can see that particle tagged to the large jet is more deflected from the jet itself if the p_{T} of the large jet is lower. That corresponds with kinematics. Let us compare several jet properties for inclusive jets and

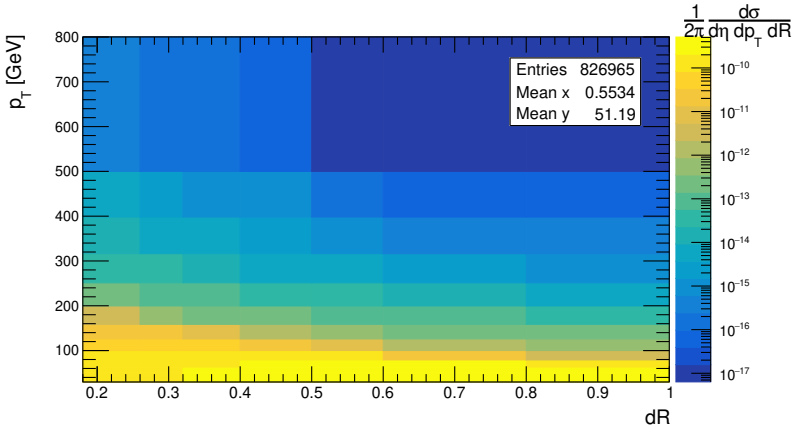

Figure 4.9: Two-dimensional distribution of p_{T} versus dR between particle tagged to the large jet (first method) and the large jet axis.

with these large jets tagged to the EWB by the first and second methods. There is a much larger contribution of large jets tagged to the EWB that have more than one sub-jet compared to the inclusive QCD sample. It is most significant for large jets consisting of three sub-jets. With a higher number of sub-jets, the ratio of tagged jets with respect to inclusive jets goes down. That can be seen in Fig. 4.10. The biggest fraction of the large jets tagged to the EWB has $\sqrt{d_{12}}$ between values $30 - 80\,\mathrm{GeV}$, which could be seen in Fig. 4.11 on the left, and on the right we can see a comparison of dR_{12} for different classes of $R = 1.0$ jets. Tagged jets to EWB, especially by the first method, tend to have higher values of dR_{12} than those of all large jets. As we can see in Fig. 4.7, there is a strong

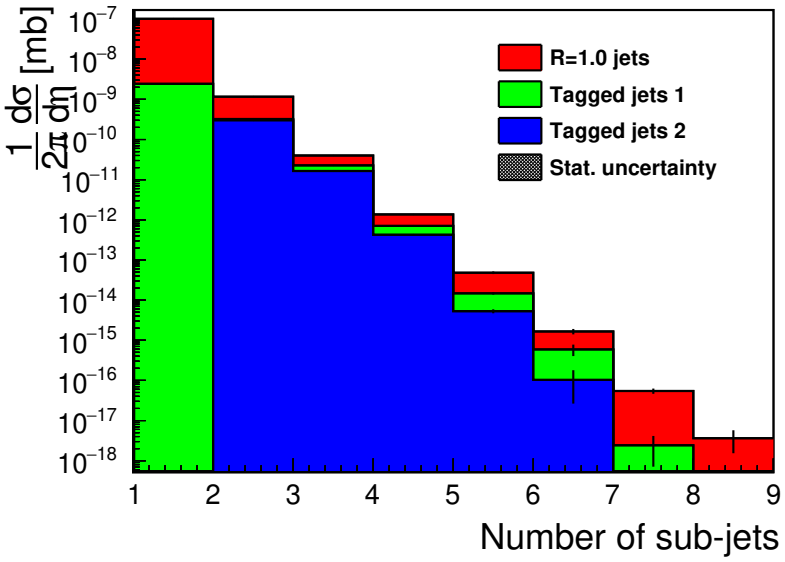

Figure 4.10: Graph comparing number of sub-jets in large $R = 1.0$ for inclusive jets (red), jets tagged to EWB by the first method (green) and by the second method (blue), all from EWB sample.

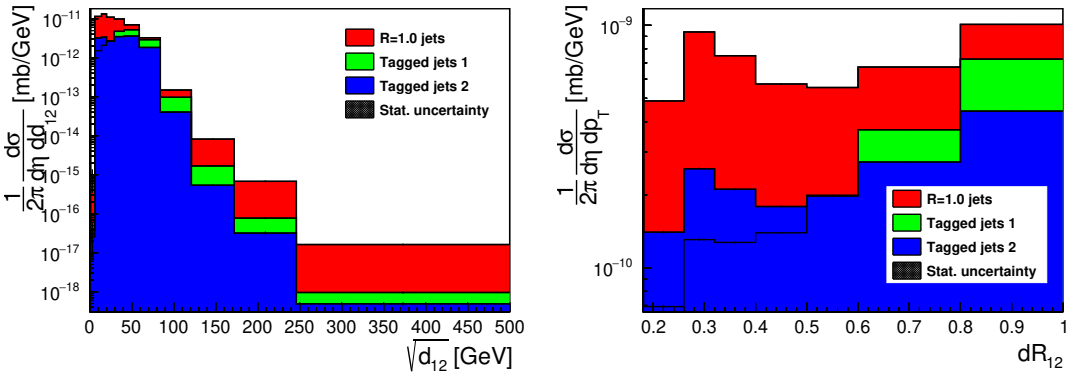

Figure 4.11: Comparison of $\sqrt{d_{12}}$ (left) and dR_{12} (right) of large $R = 1.0$ jets in general (red), tagged to EWB by first method (green) and by second method (blue), all from EWB sample.

dependence of the two jet sub-structure variables on the jet p_{T}. Let us compare the $\sqrt{d_{12}}$ and dR_{12} of large $R = 1.0$ jets for different p_{T} thresholds in the 4.12. In the panel on the left, we can see that contribution at high $\sqrt{d_{12}}$ is dominated by high p_{T} jets. On the other hand, jets with high p_{T} (like $> 400\,\mathrm{GeV}$) could still have very small $\sqrt{d_{12}}$ as well if the dR_{12} is small enough. In the figure 4.12 on the right, we can see a narrowing of the distribution with increasing jet p_{T} as one would expect from the effect of the boost. The two-dimensional histograms in Fig. 4.13 present the same quantities as 4.7 but only for large jets tagged by the second method to EWB. At the bottom histogram, we can see two structures. The contribution at low p_{T} and low dR_{12} is expected to be a background. The second structure with exponential-like behavior at higher pT is consistent with the signal of Z and W bosons. This shape is given by the equation 2.12 from chapter 2.3.4. From the kinematics, which describes that

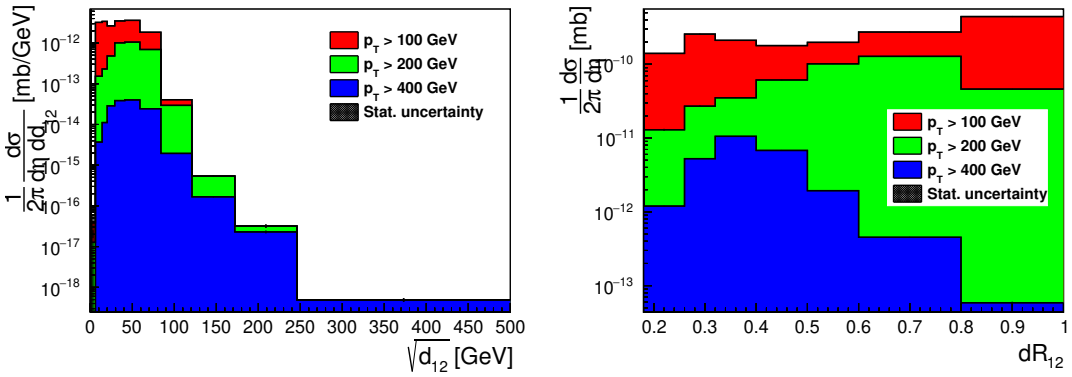

Figure 4.12: Comparison of $\sqrt{d_{12}}$ (left) and dR_{12} (right) distributions for large $R = 1.0$ jets with different p_{T} cuts, all from EWB sample.

equation, anything below that curve in the first approximation (we considered fully symmetric decay) can not be W or Z boson. We assume the case of splitting only in the ϕ direction. Thus the real simulated signal is above the curve and not only on the line because the η separation contributes to the dR by definition in eq. 1.11. We can use this eq. 2.12 as an additional requirement to the large jets, effectively decreasing the QCD background contribution. Let us compare large jets with this additional requirement, large jets tagged to the EWB and all large jets. The comparison is shown in Fig. 4.14, from which we can see that all jets with $\sqrt{d_{12}} > 100\,\mathrm{GeV}$ meets this condition. We see a large decrease in the low mass region dominated by the background on the left panel of Fig. 4.14. Change in the p_{T} spectrum can be seen in the attachment Fig. 30.

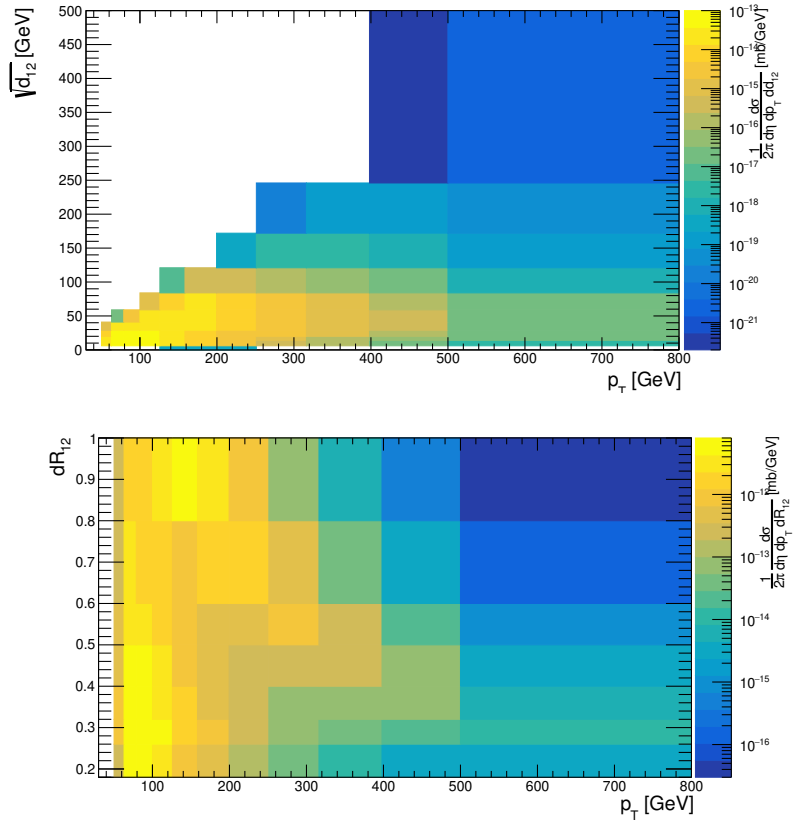

Figure 4.13: Dependence of distributions of $\sqrt{d_{12}}$ (top) and dR_{12} (down) on the p_{T} of large $R = 1.0$ tagged to EWB (second method). EWB sample is used.

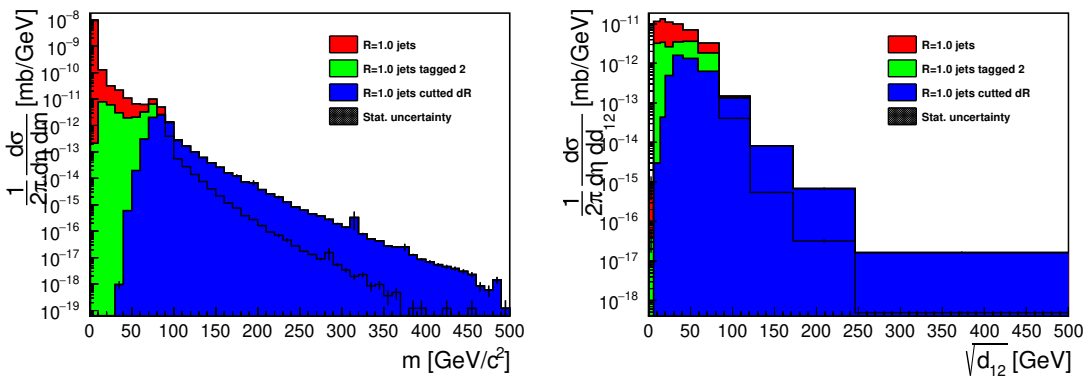

Figure 4.14: Graph comparing mass (left) and $\sqrt{d_{12}}$ (right) of large $R = 1.0$ jets with additional dR requirement to all large jets and jets tagged to electroweak bosons. EWB sample is used.

4.3 Estimation of cross-sections with increasing $\sqrt{s_{NN}}$ in collision

One of our goals is to estimate the increase in the cross-section of some processes with EWB production with an increase of the $\sqrt{s_{NN}}$ that is expected in future runs at the LHC. We will examine two scenarios of the increase in the collision energy: 1) to 5.36 TeV, which is expected in Run3, and 2) to 5.50 TeV, which is the maximum designed energy of LHC for *PbPb*. The dependence of number of jets on the collision energy is shown in Fig. 4.15 We can observe increasing change with the increasing number of jets in the event. Fig.4.16 compares pseudorapidity

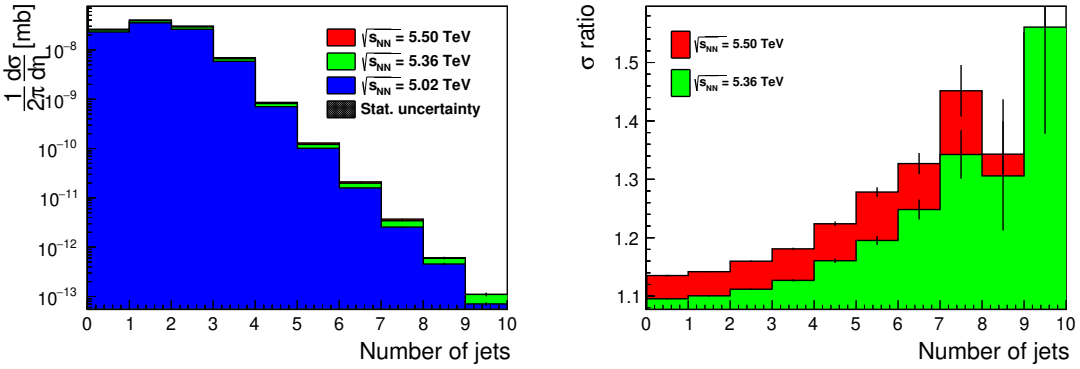

Figure 4.15: Jet cross-section as a function of the number of jets in the event for different $\sqrt{s_{NN}}$ (left) and a ratio with respect to distribution at $\sqrt{s_{NN}} = 5.02$ TeV (right) with EWB sample.

distributions of large jets above 30 GeV at higher beam energies with respect to 5.02. TeV. In the case of the QCD sample on the left, the increase in η is equally distributed across the entire interval. This contrasts with the right plot for EWB sample, where a larger increase is seen in the more forward regions. This asymmetry persists through tagging of the large jets to EWB, as we can see in Fig. 4.17. Other histograms connected to this chapter are in the attachments B,

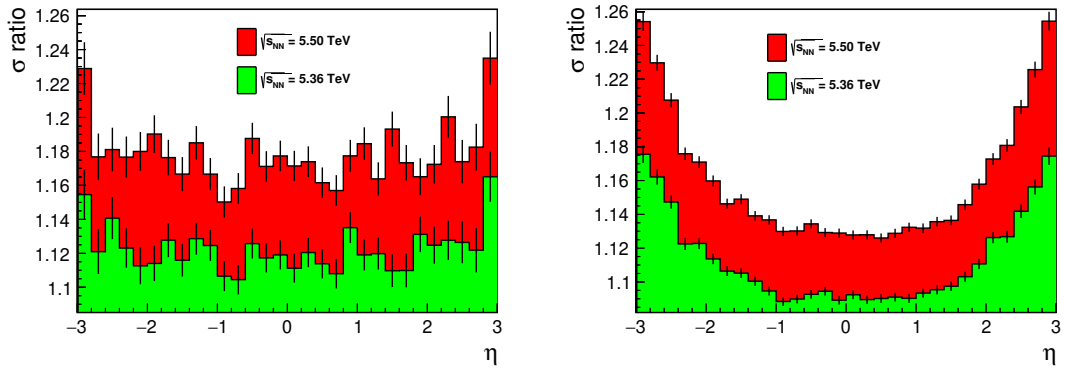

Figure 4.16: Ratio of jet cross-sections as a function of η of large $R = 1.0$ jets at two different $\sqrt{s_{NN}}$ with respect to that at $\sqrt{s_{NN}} = 5.02$ TeV. QCD sample is used on the left, and EWB sample is used on the right.

where in the Fig. 22, 23, and 24 we can see η and p_{T} distributions with the units

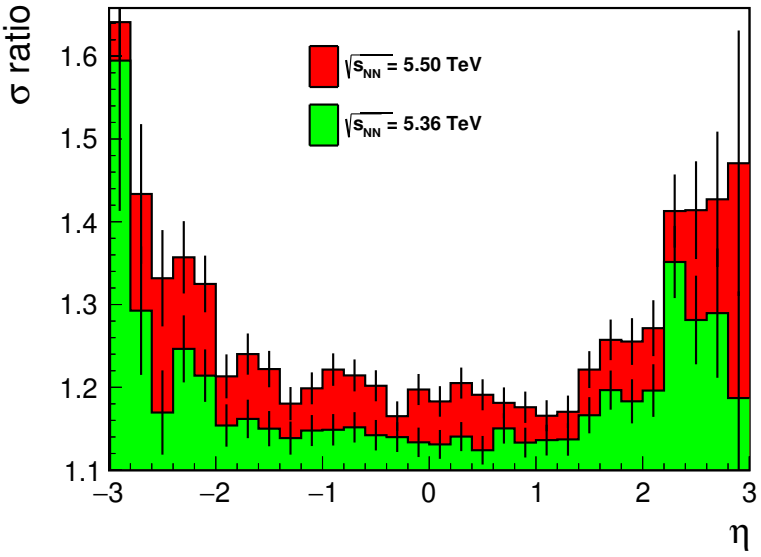

Figure 4.17: Ratio of jet cross-sections as a function of η of large $R = 1.0$ jets tagged to EWB (second method) at two different $\sqrt{s_{NN}}$ with respect to that at $\sqrt{s_{NN}} = 5.02\,\text{TeV}$. EWB sample is used.

of cross-section respectively. An increase of the cross-section with the increase of $\sqrt{s_{NN}}$ is higher for large jets with higher $\sqrt{d_{12}}$, which could be seen in the Fig. 4.18. In the right panel, we could see suppression to 1/5 in the first bin $(0 - 6\,\text{GeV})$. This bin is, however, on the edge of the kinematic limit and only sparsely populated. Change of the cross-section in the case of tagged large jets

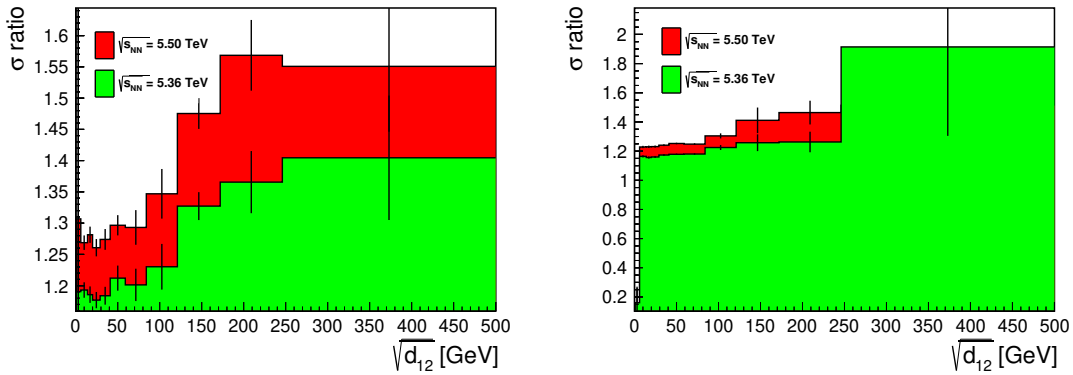

Figure 4.18: Ratios of cross-sections as a function of $\sqrt{d_{12}}$ of large $R = 1.0$ jets (re-clustered with k_T algorithm) at two different $\sqrt{s_{NN}}$ to that at $\sqrt{s_{NN}} = 5.02\,\text{TeV}$. QCD sample is used on the left, and EWB sample is used on the right.

(second method) is not highly depending on the $\sqrt{d_{12}}$ or dR_{12} as we can see in Fig. 4.19. It seems that for higher $\sqrt{d_{12}}$, the ratio of cross-sections increases, but the increase is within statistical uncertainties. The increase around 150 GeV is expected to originate from the cross-section weighting of the different MC samples. The σ ratio increase is slightly more significant in the center of dR_{12} interval (could be just statistical fluctuation), as shown in Fig. 4.19 - in contrast with the case of all large jets 29, which has a uniform spectrum. An important goal is to try to estimate the number of jets with specific p_{T} , which will be seen

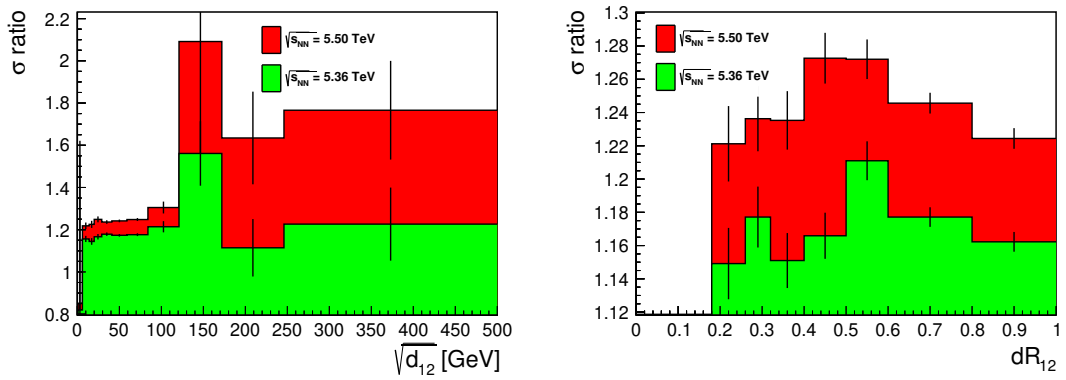

Figure 4.19: Ratios of cross-sections as a function of $\sqrt{d_{12}}$ of large $R = 1.0$ jets tagged to EWB (second method) at two different $\sqrt{s_{NN}}$ to that at $\sqrt{s_{NN}} = 5.02\,\text{TeV}$. EWB sample is used.

in the next run of heavy ion collision at ATLAS. The increase of the cross-section is much higher with increasing p_{T} , which could be seen in Fig. 4.20 for inclusive jets. Nevertheless, the increase seen in the EWB sample is slightly higher at higher p_{T} than in the QCD sample. An overall increase of the jet cross-section by 15% and 35% is expected to be seen in Run3 at the LHC for jets with 100 GeV, and 500 GeV, respectively. Similar behavior in p_{T} spectrum of large $R = 1.0$ jets

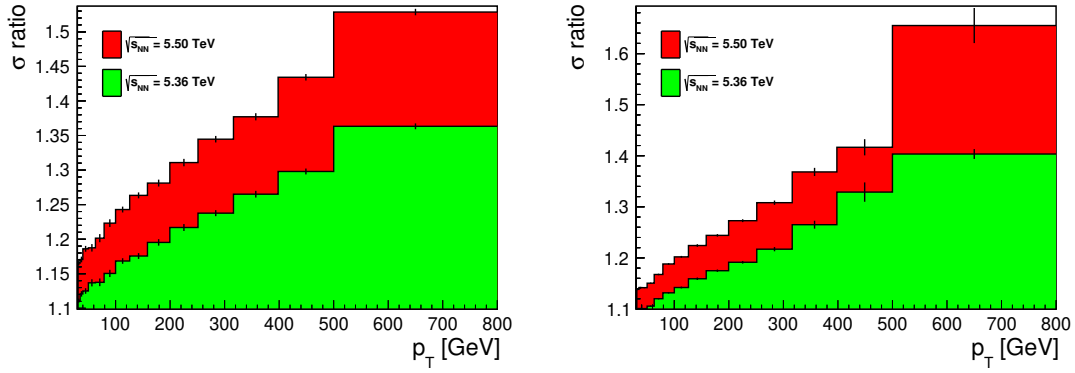

Figure 4.20: Ratios of inclusive jet cross-sections of large $R = 1.0$ jets at two different $\sqrt{s_{NN}}$ to that at $\sqrt{s_{NN}} = 5.02\,\text{TeV}$. QCD sample is used on the left, and EWB sample is used on the right.

is also seen for large jets tagged to EWB (second method), see Fig. 4.21, except anomaly in low p_{T} , probably hence lower statistic of low p_{T} tagged to EWB.

For different samples and objects, let us integrate cross-sections over the interval $p_{\text{T}} \in (100, 800)\,\text{GeV}$, to be able to estimate expected yields in the 2023 heavy ion run. Results are written in the tab. 4.3. The difference of p_{T} spectra, which we integrated, can be seen in Fig. 30 in attachments.

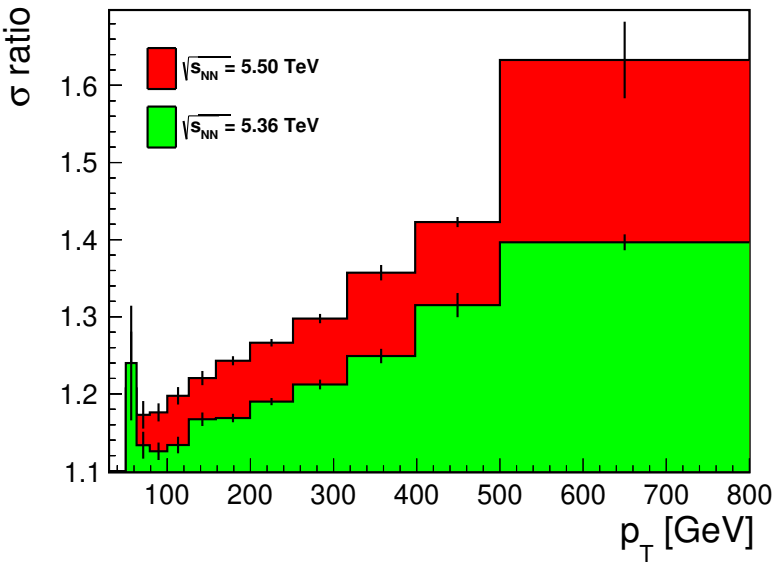

Figure 4.21: Ratios of inclusive jet cross-sections of large $R = 1.0$ jets tagged to EWB (second method) at two different $\sqrt{s_{NN}}$ to that at $\sqrt{s_{NN}} = 5.02\,\text{TeV}$.

$\sqrt{s_{NN}}$ [TeV]	**5.02**	**5.36**	**5.50**
Inclusive	56.190	65.981	70.437
Tagged 1	$3.038 \cdot 10^{-2}$	$3.516 \cdot 10^{-2}$	$3.712 \cdot 10^{-2}$
Tagged 2	$8.456 \cdot 10^{-3}$	$9.893 \cdot 10^{-3}$	$10.478 \cdot 10^{-3}$
dR cuted	$2.598 \cdot 10^{-3}$	$3.147 \cdot 10^{-3}$	$3.363 \cdot 10^{-3}$

Table 4.3: Values of cross-section σ of large $R = 1.0$ jets with $p_{\text{T}} \in (100, 800)$ GeV integrated over the whole ϕ interval and $|\eta| < 3$. The cross-section is in units nb (nano-barn).

Let us compute expected number N of jets of different types given by their cross-section σ with modified equation (1.3):

$$N = L_{\text{int}} \cdot A^2 \cdot \sigma, \tag{4.1}$$

where L_{int} is the expected integrated luminosity. It is estimated to be $3\,\text{fb}^{-1}$ for the 2023 heavy ion run on ATLAS, A is the atomic number ($A(^{208}_{82}Pb) = 208$. Our simulations work as pp collisions with the equivalent energy of heavy ion collisions. Hence we need to add factor A^2 to our cross-section. Results are written in the tab. 4.4.

$\sqrt{s_{NN}}$ [TeV]	**5.02**	**5.36**	**5.50**
Inclusive	7 220 000	8 510 000	9 090 000
Tagged 1	3 920	4 540	4 790
Tagged 2	1 090	1 160	1 350
dR cuted	340	410	430

Table 4.4: Number of different types of jets estimated to be observed in the 2023 heavy-ion run (considered centrality: $0 - 100\%$).

Conclusion

In the thesis, we summarize basic information about the detector setup in the ATLAS experiment and provide a brief description of the physics of quark-gluon plasma and heavy-ion collisions. We compute some relations concerning the behavior of the electro-weak bosons in the QGP, coming to the conclusion that in the current energetic range of the ATLAS experiment, we can not expect decays of EWB in the formed plasma, and with the expected luminosity, they can not be used to probe time evolution of QGP. On the other hand, the short lifetime of EWB, as we computed, ensures the interaction of quarks from EWB decay with QGP.

We simulated samples with and without the process leading to EWB formation. From the study of re-clustering jets with $R = 1.0$, we can assume a better performance finding signal of EWB in these large jets than in the invariant mass of inclusive $R = 0.2$ jets. We study two different methods of tagging these large jets and compare their performances. The second method, which uses the parenthood of particles tagged to two sub-jets, provides results of higher purity but leads to lower yields. Since these methods describe different physical decay scenarios, they could be used complementary.

We derive the formula for minimum dR_{12} of large jets coming from EWB with the dependence of the p_{T} of large jets. That could be used as a selection criterion to eliminate low p_{T} background. We observe the effective separation of signal from background, but the efficiency of this cut needs to be further studied.

Both samples have been generated with three different values of center-of-mass energy to predict the increase in cross-section in future data taking. Based on our simulation, an increase of the large jet cross-section by 15% and 35% is expected to be seen in Run3 at the LHC for jets above 100 GeV and 500 GeV, respectively. As a final result, we calculate the expected number of different jets in the run 2 of heavy-ion collisions. These results are for inclusive large jets as well as tagged large jets to EWB by different methods.

Bibliography

[1] *CERN experiments*. URL: https://home.cern/science/experiments (visited on 02/01/2023).

[2] *Facts and figures about LHC, CERN*. URL: https://home.cern/resources/faqs/facts-and-figures-about-lhc (visited on 02/16/2023).

[3] *SYNCHROTRON RADIATION, R.P. Walker, Sincrotrone Trieste, Italy*. eq. n. (6). URL: https://cds.cern.ch/record/398429/files/p437.pdf (visited on 03/21/2023).

[4] *Particle interaction in detector layers*. URL: http://cds.cern.ch/record/1323010/plots (visited on 03/08/2023).

[5] *Public ATLAS Luminosity Results for Run-2 of the LHC*. URL: https://twiki.cern.ch/twiki/bin/view/AtlasPublic/LuminosityPublicResultsRun2 (visited on 03/22/2023).

[6] *Public ATLAS Luminosity Results for Run-3 of the LHC*. URL: https://twiki.cern.ch/twiki/bin/view/AtlasPublic/LuminosityPublicResultsRun3 (visited on 03/22/2023).

[7] *Diagram of ATLAS detector*. URL: https://cds.cern.ch/record/39038 (visited on 03/08/2023).

[8] *ATLAS coordinate system, picture*. TikZ, by Izaak Neutelings. URL: https://tikz.net/wp-content/uploads/2021/09/axis3D_CMS-003.png (visited on 03/22/2023).

[9] M. Tanabashi et al. (Particle Data Group). "REVIEW OF PARTICLE PHYSICS". In: (2018). DOI: 10.1103/PhysRevD.98.030001.

[10] *ATLAS Inner tracker diagram*. URL: https://cds.cern.ch/images/CERN-GE-0803014-01 (visited on 03/08/2023).

[11] *ATLAS inner tracker information, CERN web*. URL: https://atlas.cern/Discover/Detector/Inner-Detector (visited on 03/08/2023).

[12] *ATLAS inner tracker diagram view from r-z plane*. URL: https://www.researchgate.net/figure/The-inner-detector-of-the-ATLAS-experiment-during-the-first-LHC-data-taking-period-in_fig1_316705875 (visited on 03/08/2023).

[13] *ATLAS SCT strip sensor - schematic view*. URL: https://www.researchgate.net/figure/Schematics-showing-a-single-sided-AC-coupled-silicon-strip-detector-After-42_fig5_296683651 (visited on 03/08/2023).

[14] *ATLAS magnet system*. Search for the Higgs Boson in the Process pp to Hqq, H to WW with the ATLAS Detector - Scientific Figure on ResearchGate. URL: https://www.researchgate.net/figure/Sketch-of-the-ATLAS-magnet-system-with-the-central-solenoid-and-the-three-toroids_fig4_42427478 (visited on 03/22/2023).

[15] *The ATLAS Experiment at the CERN Large Hadron Collider*. IOP Publishing Ltd and SISSA, 2008. URL: https://cds.cern.ch/record/1129811/files/jinst8_08_s08003.pdf.

[16] *Magnet system of ATLAS detector, CERN*. URL: https://atlas.cern/Discover/Detector/Magnet-System (visited on 03/22/2023).

[17] *ATLAS calorimeter, CERN website*. URL: https://atlas.cern/Discover/Detector/Calorimeter (visited on 03/22/2023).

[18] Nikiforos (Columbia U.) Nikiforou. *Performance of the ATLAS Liquid Argon Calorimeter after three years of LHC operation and plans for a future upgrade*. URL: https://cds.cern.ch/record/1558820 (visited on 03/22/2023).

[19] Bernardo (Juiz de Fora U.) Sotto-Maior Peralva. *Calibration and Performance of the ATLAS Tile Calorimeter*. URL: https://cds.cern.ch/record/1545496 (visited on 03/22/2023).

[20] S. Grinstein. "The ATLAS Forward Proton Detector (AFP)". In: *Nuclear and Particle Physics Proceedings* 273-275 (2016). 37th International Conference on High Energy Physics (ICHEP), pp. 1180–1184. ISSN: 2405-6014. DOI: https://doi.org/10.1016/j.nuclphysbps.2015.09.185. URL: https://www.sciencedirect.com/science/article/pii/S2405601415006744.

[21] *Generated image of ATLAS Muon Spectrometer*. URL: https://cds.cern.ch/record/1095929 (visited on 04/19/2023).

[22] *Trigger menu in 2018*. Tech. rep. All figures including auxiliary figures are available at https://atlas.web.cern.ch/Atlas/GROUPS/PHYSICS/PUBNOTES/ATL-DAQ-PUB-2019-001. Geneva: CERN, 2019. URL: https://cds.cern.ch/record/2693402.

[23] M Rybar. *Triggering on jets in heavy ion collisions at the ATLAS experiment*. Tech. rep. 31.3.2009. Geneva: CERN, 2009. URL: http://cds.cern.ch/record/1168019.

[24] *Standard Model of Particle Physics, CERN datafile system*. URL: https://cds.cern.ch/record/2315477/plots#0 (visited on 04/20/2023).

[25] A. D. Martin et al. "Parton distributions for the LHC". In: *Eur. Phys. J. C* 63 (2009), pp. 189–285. DOI: 10.1140/epjc/s10052-009-1072-5. arXiv: 0901.0002 [hep-ph].

[26] Krishna Rajagopal Wit Busza and Wilke van der Schee. "Heavy Ion Collisions: The Big Picture, and the Big Questions". In: *Nucl. Part. Sci.* (2018). arXiv: 1802.04801v2 [hep-ph].

[27] Eskola Kari J. et al. "EPPS21: a global QCD analysis of nuclear PDFs". In: *The European Physical Journal C* (2022). ISSN: 1434-6052. URL: https://doi.org/10.1140/epjc/s10052-022-10359-0.

[28] LHCb Collaboration. "Centrality determination in heavy-ion collisions with the LHCb detector". In: (Nov. 2021). DOI: 10.1088/1748-0221/17/05/P05009. arXiv: 2111.01607.

[29] I. Angeli and K.P. Marinova. "Table of experimental nuclear ground state charge radii: An update". In: *Atomic Data and Nuclear Data Tables* 99.1 (2013), pp. 69–95. ISSN: 0092-640X. DOI: https://doi.org/10.1016/j.adt.2011.12.006. URL: https://www.sciencedirect.com/science/article/pii/S0092640X12000265.

[30] ATLAS experiment. In: *Physics Letters B* 802 (Mar. 2020), p. 135262. DOI: 10.1016/j.physletb.2020.135262. URL: https://doi.org/10.1016%5C%2Fj.physletb.2020.135262.

[31] ATLAS experiment. "Centrality, rapidity and transverse momentum dependence of isolated prompt photon production in lead-lead collisions at $\sqrt{s_{NN}}$ = 2.76 TeV measured with the ATLAS detector". In: *Physical Review C* 93.3 (Mar. 2016). DOI: 10.1103/physrevc.93.034914. URL: https://doi.org/10.1103%5C%2Fphysrevc.93.034914.

[32] Saraswati Pandey and Bhartendu Singh. "Transverse momentum spectra and suppression of charged hadrons in deformed Xe-Xe collisions at $\sqrt{s_{NN}}$ = 5.44 TeV using HYDJET++ model". In: (Oct. 2022). DOI: 10.48550/arXiv.2210.08527.

[33] J. D. Bjorken. "Highly relativistic nucleus-nucleus collisions: The central rapidity region". In: *Phys. Rev. D* 27 (1 Jan. 1983), pp. 140–151. DOI: 10.1103/PhysRevD.27.140. URL: https://link.aps.org/doi/10.1103/PhysRevD.27.140.

[34] Wilke van der Schee, Paul Romatschke, and Scott Pratt. "Fully Dynamical Simulation of Central Nuclear Collisions". In: *Physical Review Letters* 111.22 (Nov. 2013). DOI: 10.1103/physrevlett.111.222302. URL: https://doi.org/10.1103%2Fphysrevlett.111.222302.

[35] Leticia Cunqueiro and Anne M. Sickles. "Studying the QGP with Jets at the LHC and RHIC". In: *Progress in Particle and Nuclear Physics* 124 (May 2022), p. 103940. DOI: 10.1016/j.ppnp.2022.103940. URL: https://doi.org/10.1016%2Fj.ppnp.2022.103940.

[36] ATLAS colaboration. In: *Physics Letters B* 790 (Mar. 2019), pp. 108–128. DOI: 10.1016/j.physletb.2018.10.076. URL: https://doi.org/10.1016%2Fj.physletb.2018.10.076.

[37] Matteo Cacciari, Gavin P Salam, and Gregory Soyez. "The anti-k_T jet clustering algorithm". In: *Journal of High Energy Physics* 2008.04 (Apr. 2008), pp. 063–063. DOI: 10.1088/1126-6708/2008/04/063. URL: https://doi.org/10.1088%2F1126-6708%2F2008%2F04%2F063.

[38] Christian Bierlich et al. *A comprehensive guide to the physics and usage of PYTHIA 8.3*. 2022. arXiv: 2203.11601 [hep-ph].

[39] *Monte Carlo Simulation, Wikipedia*. URL: https://en.wikipedia.org/wiki/Monte_Carlo_method (visited on 05/06/2023).

[40] *Pythia 8, Particle Properties*. URL: https://pythia.org/latest-manual/ParticleProperties.html (visited on 05/06/2023).

List of Figures

List of Tables

Attachments

A. Pythia settings

```
// ******** Pythia collision configurations *********
pythia.readString("Main:numberOfEvents = 5000000");
// Number of collisions to be generated
pythia.readString("HardQCD:all = on");
// Used as an option "QCD"
pythia.readString("WeakDoubleBoson:all = on");
pythia.readString("WeakBosonAndParton:all = on");
// Both used as an option "EWB"
pythia.readString( Form("PhaseSpace:pTHatMin= %.0f", pTHatMin) );
//hardness of the collision - lower limit
pythia.readString( Form("PhaseSpace:pTHatMax= %.0f", pTHatMax) );
//hardness of the collision - upper limit

//other settings
pythia.readString("Beams:eCM = 5020.");  // Collisions energy
pythia.readString("Main:timesAllowErrors = 10");
pythia.readString("Random:setSeed = on");
pythia.readString("Init:showAllSettings = off");
pythia.readString("Init:showChangedParticleData = on");
pythia.readString("Init:showAllParticleData = off");

// common ATLAS Pythia8
pythia.readString("Main:timesAllowErrors = 500");
pythia.readString("6:m0 = 172.5");
pythia.readString("23:m0 = 91.1876");
pythia.readString("23:mWidth = 2.4952");
pythia.readString("24:m0 = 80.399");
pythia.readString("24:mWidth = 2.085");
pythia.readString("StandardModel:sin2thetaW = 0.23113");
pythia.readString("StandardModel:sin2thetaWbar = 0.23146");
pythia.readString("ParticleDecays:limitTau0 = on");
pythia.readString("ParticleDecays:tau0Max = 10.0");

// CT10 + AU2 tune
pythia.readString("Tune:pp = 5");
pythia.readString("MultipartonInteractions:bProfile = 4");
pythia.readString("MultipartonInteractions:a1 = 0.10");
pythia.readString("MultipartonInteractions:pT0Ref = 1.70");
pythia.readString("MultipartonInteractions:ecmPow = 0.16");
pythia.readString("SpaceShower:rapidityOrder=0");

// CALL PYGIVE(MSTP(81)=0)
pythia.readString("PartonLevel:MPI = off");
```

B. Additional plots

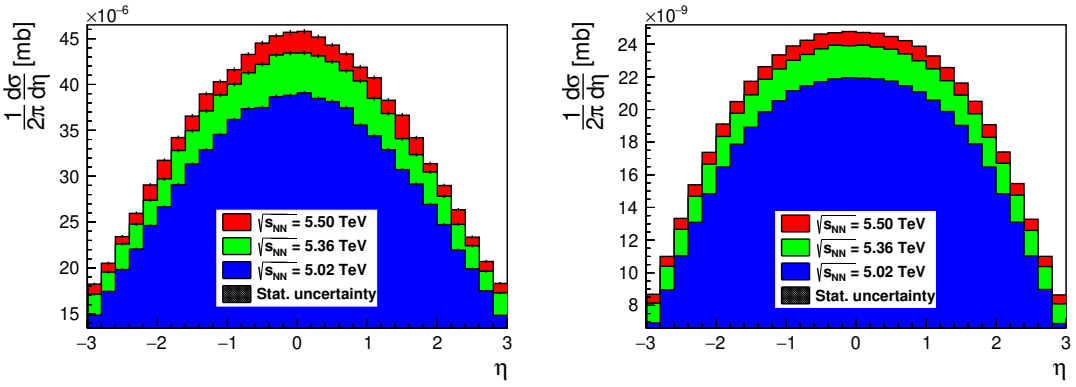

Figure 22: Graphs of η angle of large $R = 1.0$ jets with different $\sqrt{s_{NN}}$ used in generation with QCD sample (left) and EWB sample (right).

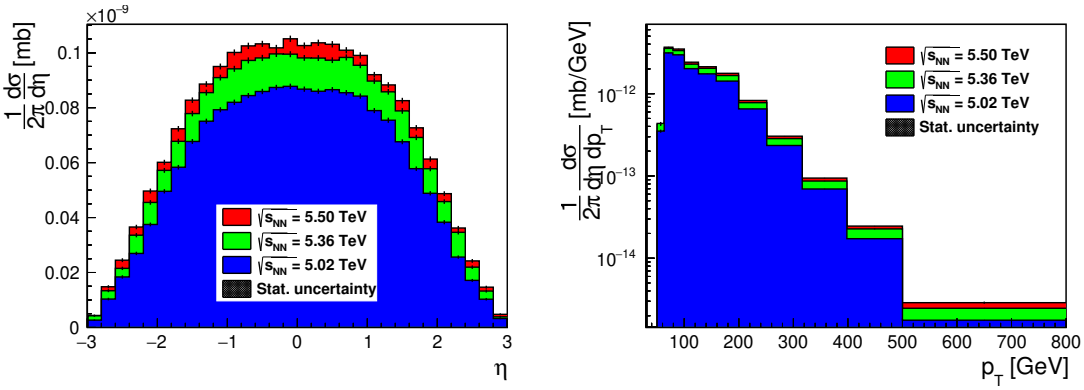

Figure 23: Graphs of η angle (left) and p_{T} (right) of large $R = 1.0$ jets tagged to EWB (second method) with different $\sqrt{s_{NN}}$ used in generation with EWB.

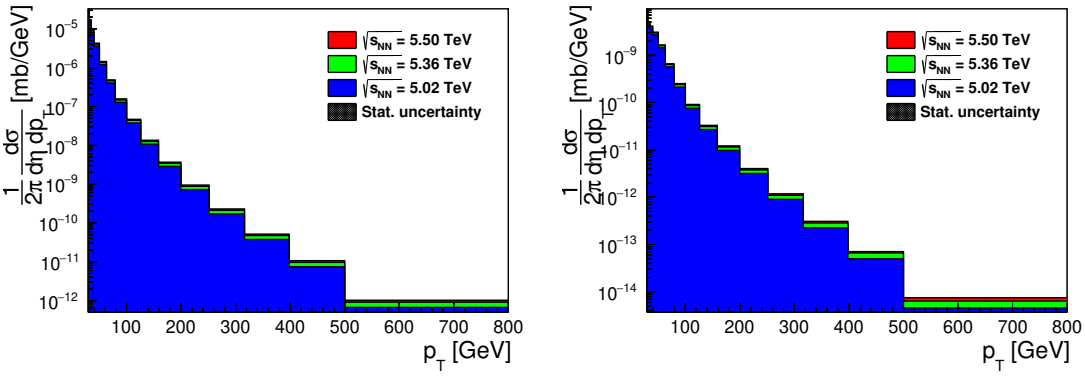

Figure 24: Graphs of p_{T} of large $R = 1.0$ jets from QCD sample (left) and EWB sample (right) with different $\sqrt{s_{NN}}$ used in generation.

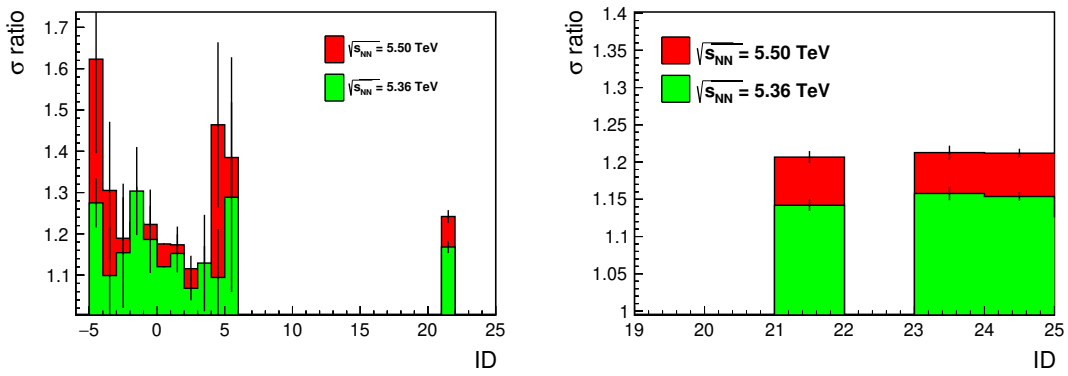

Figure 25: Graph of particle ID tagged to large $R = 1.0$ jet (second method) to σ ratio of different $\sqrt{s_{NN}}$ samples drawn to sample with $\sqrt{s_{NN}} = 5.02\,\text{TeV}$. QCD sample on the left and EWB sample on the right.

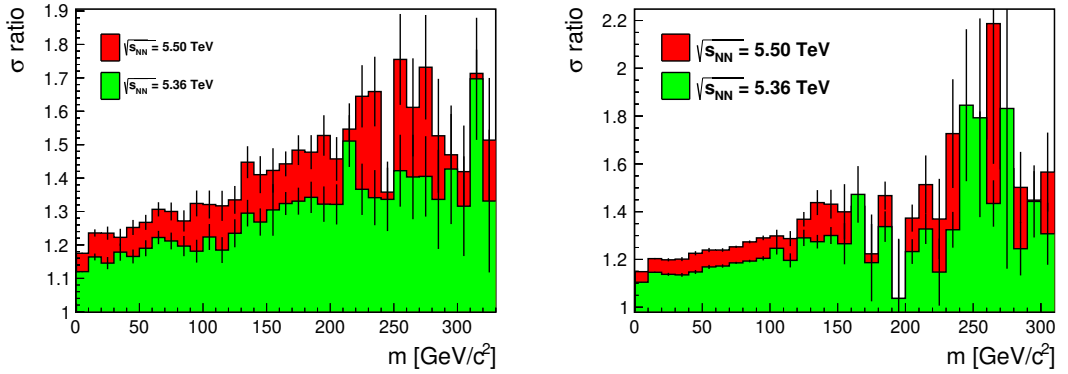

Figure 26: Graph of mass of the large $R = 1.0$ jet to σ ratio of different $\sqrt{s_{NN}}$ samples drawn to sample with $\sqrt{s_{NN}} = 5.02\,\text{TeV}$. QCD sample on the left and EWB sample on the right.

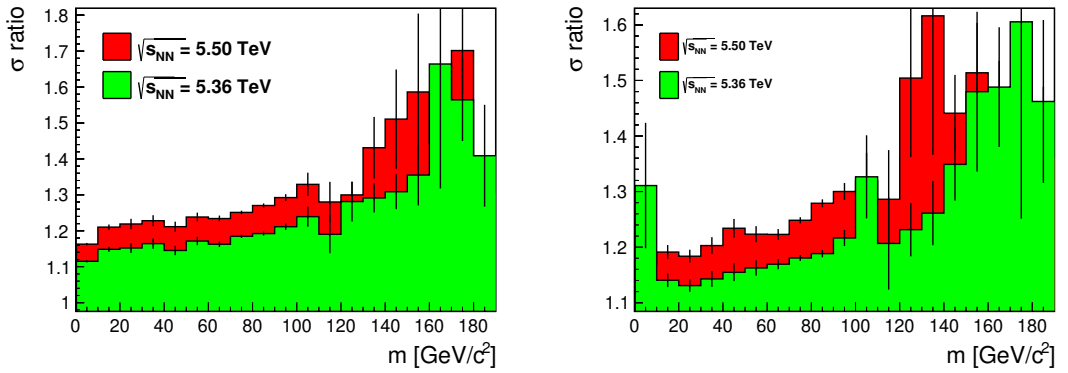

Figure 27: Graph of large $R = 1.0$ jet tagged to EWB to σ ratio of different $\sqrt{s_{NN}}$ samples drawn to sample with $\sqrt{s_{NN}} = 5.02\,\text{TeV}$. Jets tagged by the first method is on the left and by the second method on the right.

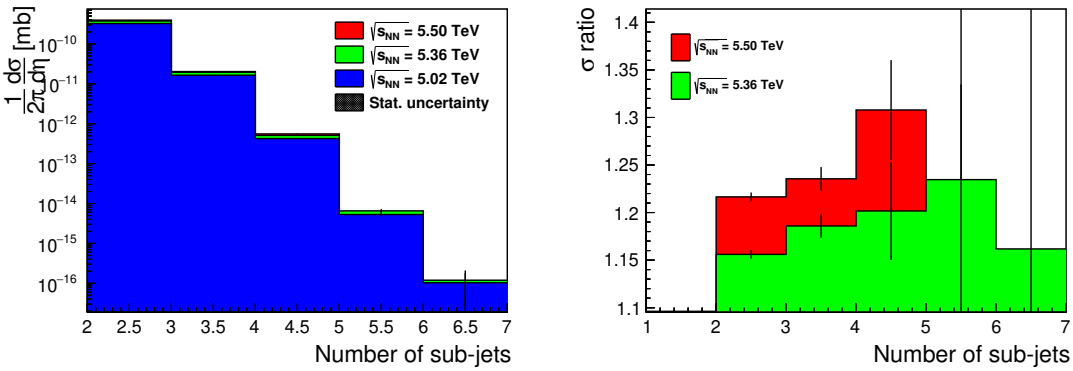

Figure 28: Graph of a number of sub-jets of the large $R = 1.0$ jet tagged to the EWB (second method). The differential cross-section is shown on the left, and *sigma* ratio of different $\sqrt{s_{NN}}$ samples drawn to sample with $\sqrt{s_{NN}} = 5.02\,\mathrm{TeV}$ is shown on the right.

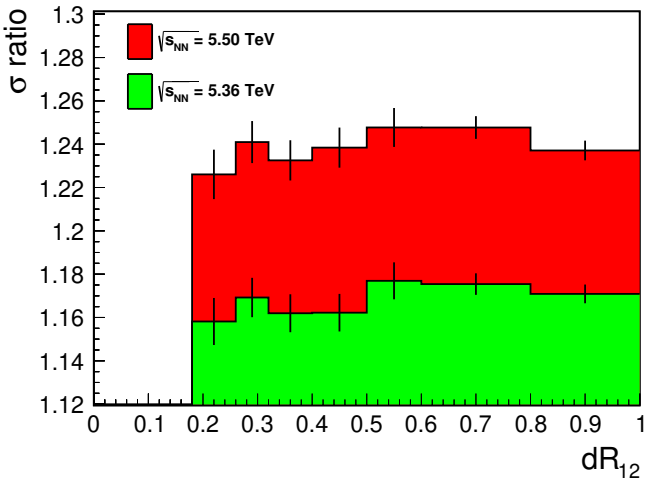

Figure 29: Graph comparing dR_{12} of large $R = 1.0$ jets (re-clustered with k_T algorithm) of different $\sqrt{s_{NN}}$ samples drawn to sample with $\sqrt{s_{NN}} = 5.02\,\mathrm{TeV}$, EWB sample is used.

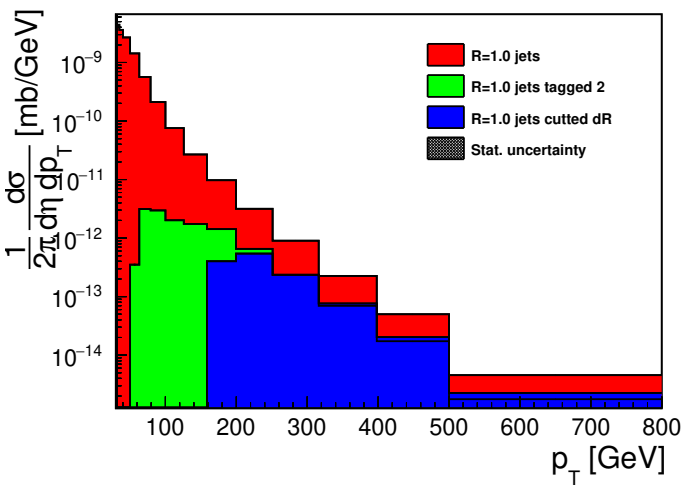

Figure 30: Graph comparing dR_{12} of large $R = 1.0$ jets (re-clustered with k_T algorithm) of different $\sqrt{s_{NN}}$ samples drawn to sample with $\sqrt{s_{NN}} = 5.02\,\mathrm{TeV}$, EWB sample is used.